Graphical Abstract

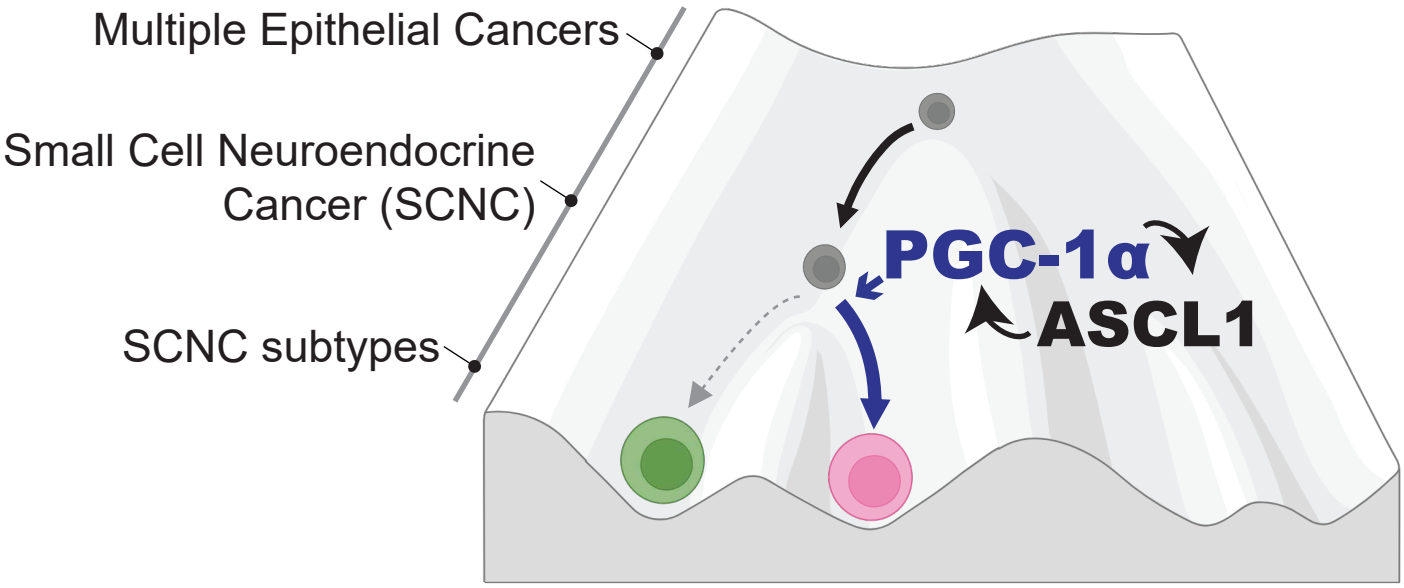

SCNC subtypes	POU2F3/ ASCL2	ASCL1
Metabolic Heterogeneity	↓ PGC-1α	↑ PGC-1α
	↓ OXPHOS	↑ OXPHOS
	↓ Metabolic Plasticity	↑ Metabolic Plasticity
Metabolic Vulnerability	↑↑ Sensitivity to OXPHOS Inhibition	↑ Sensitivity to OXPHOS Inhibition

PGC-1α drives small cell neuroendocrine cancer progression towards an ASCL1-expressing subtype with increased mitochondrial capacity

Grigor Varuzhanyan[1,**], Chia-Chun Chen[2], Jack Freeland[2,3], Tian He[2], Wendy Tran[1], Kai Song[4], Liang Wang[1], Donghui Cheng[5], Shili Xu[2,7,12], Gabriella A. Dibernardo[5,10], Favour N Esedebe[6], Evan R. Abt[2], Jung Wook Park[8], Sanaz Memarzadeh[9,10,11,12,13], Thomas Graeber[2,5,7,12,14,15], Orian Shirihai[2,3,16,17], Owen Witte[1,2,5,12,13,18,*]

1. Department of Microbiology Immunology and Molecular Genetics, University of California, Los Angeles (UCLA), CA, USA
2. Department of Molecular and Medical Pharmacology, UCLA, CA, USA
3. Molecular Biology Interdepartmental Program, UCLA, CA, USA
4. Department of Bioengineering, UCLA, CA, USA
5. Eli and Edythe Broad Stem Cell Research Center, UCLA, CA, USA
6. Bioinformatics Interdepartmental Program, UCLA, CA, USA
7. Crump Institute for Molecular Imaging, David Geffen School of Medicine, UCLA, CA, USA
8. Department of Pathology, Duke University School of Medicine, Durham, NC, USA
9. Eli and Edythe Broad Center of Regeneration Medicine and Stem Cell Research, UCLA, CA, USA
10. Department of Obstetrics and Gynecology, David Geffen School of Medicine, UCLA, CA, USA
11. The VA Greater Los Angeles Healthcare System, Los Angeles, CA, USA
12. Jonsson Comprehensive Cancer Center, the David Geffen School of Medicine, UCLA, CA, USA
13. Molecular Biology Institute, UCLA, CA, USA
14. California NanoSystems Institute, UCLA, CA, USA
15. Metabolomics Center, UCLA, CA, USA
16. Division of Endocrinology, Department of Medicine, David Geffen School of Medicine, UCLA, CA 90095, USA
17. Department of Clinical Biochemistry, School of Medicine, Ben Gurion University of The Negev, Beer-Sheva, Israel
18. Parker Institute for Cancer Immunotherapy, UCLA, CA, USA

Corresponding Author Emails
*Owen N. Witte: owenwitte@mednet.ucla.edu
**Grigor Varuzhanyan: gvaruzhanyan@mednet.ucla.edu

Keywords: PGC-1α; ASCL1; ASCL2; POU2F3; OXPHOS; lineage plasticity; small cell neuroendocrine; prostate cancer; lung cancer

SUMMARY

Adenocarcinomas from multiple tissues can converge to treatment-resistant small cell neuroendocrine (SCN) cancers comprised of ASCL1, POU2F3, NEUROD1, and YAP1 subtypes. We investigated how mitochondrial metabolism influences SCN cancer (SCNC) progression. Extensive bioinformatics analyses encompassing thousands of patient tumors and human cancer cell lines uncovered enhanced expression of PGC-1α, a potent regulator of mitochondrial oxidative phosphorylation (OXPHOS), across several SCNC types. PGC-1α correlated tightly with increased expression of the lineage marker ASCL1 through a positive feedback mechanism. Analyses using a human prostate tissue-based SCN transformation system showed that the ASCL1 subtype has heightened PGC-1α expression and OXPHOS activity. PGC-1α inhibition diminished OXPHOS, reduced SCNC cell proliferation, and blocked SCN prostate tumor formation. PGC-1α overexpression enhanced OXPHOS, tripled the SCN prostate tumor formation rate, and promoted commitment to the ASCL1 lineage. These findings reveal the metabolic heterogeneity among SCNC subtypes and identify PGC-1α-induced OXPHOS as a regulator of SCNC lineage plasticity.

INTRODUCTION

Epithelial cancers from various tissues, including the prostate, lung, and bladder, can converge to an aggressive small cell neuroendocrine (SCN) phenotype under targeted treatments[1–3]. Small cell neuroendocrine cancers (SCNCs) are classified as high-grade, poorly differentiated small cell carcinomas that commonly express neuroendocrine markers like chromogranin A (CHGA), neural cell adhesion molecule 1 (NCAM1), and synaptophysin (SYP)[4]. The most common type of SCNC, small cell lung cancer (SCLC), represents around 14% of all lung cancer diagnoses. Globally, about 250,000 individuals are diagnosed with SCLC annually, with roughly 200,000 of these patients succumbing to the disease each year. Although de novo neuroendocrine prostate cancer is rare (<1% of cases), the prevalence of treatment-induced SCN prostate cancer is increasing, likely due to resistance mechanisms triggered by androgen deprivation therapy (ADT)[5,6]. This treatment-induced form of prostate cancer accounts for about 10-40% of all ADT-insensitive, castration-resistant prostate cancer (CRPC) cases.

With a limited long-term effectiveness of current chemotherapy strategies[7] indicated by a dismal median survival rate between 7-16 months[8], there is an urgent need for alternative treatment strategies.

SCNCs were traditionally seen as a uniform group of cancers but are now understood to include multiple subtypes. These subtypes, defined by their prominent expression of lineage-specific molecular markers, showcase the diversity within SCNCs. This is best exemplified in SCLC, which is categorized into ASCL1, NEUROD1, POU2F3, and YAP1 subtypes[9,10]. Recent studies have identified corresponding subtypes in SCN prostate cancer, including ASCL1, POU2F3/ASCL2, and NEUROD1[11–13]. A growing body of research across numerous SCNC models has highlighted the plastic nature of differentiation towards and between these subtypes[9,10,14,15], a feature that likely contributes to treatment resistance.

Complementing the molecular heterogeneity within SCNCs, recent studies have begun to highlight the metabolic diversity across different SCLC subtypes[16–20]. Notably, a correlation has been observed between ASCL1 expression levels and a dependence on inosine monophosphate dehydrogenase, a key enzyme in guanosine biosynthesis critical for normal metabolic functions[16]. These insights raise the possibility that metabolic reprogramming might regulate lineage plasticity in SCNCs. Indeed, metabolic reprogramming not only influences cell fate decisions[21] but is also orchestrated by oncogenes to regulate these decisions[22]. These observations highlight the intimate interplay between cancer metabolism and lineage plasticity. Specifically, SCN-associated oncogenes such as MYC[23–27], AKT[28,29], TP53[30,31], and RB1[32–34], regulate metabolic pathways individually, but their collective impact on metabolic reprogramming and lineage determination during SCNC remains unclear.

A key aspect of cancer cell metabolic reprogramming is the shift towards aerobic glycolysis (also known as the Warburg effect) characterized by an increased rate of glucose consumption and lactate secretion, even in the presence of ample oxygen[35–37]. This seminal discovery made nearly a century ago by Otto Warburg led to a longstanding belief that cancer cells have dysfunctional mitochondria. However, recent studies have countered this perspective, showing that many cancers actually have functional mitochondria fully capable of processing fuels via the tricarboxylic acid (TCA) cycle to support oxidative phosphorylation (OXPHOS)[38]. In fact, some cancers have a heightened reliance on OXPHOS[39,40], which

90 is sometimes linked with therapy resistance[41–46]. This emerging understanding has sparked significant
91 interest in OXPHOS inhibitors as promising candidates for cancer therapy[47–49].

92 Increased aerobic glycolysis has been observed in SCN prostate cancer[50], but the specific role of
93 OXPHOS in SCN transformation and lineage plasticity remains to be unraveled. Thus, we reasoned that
94 investigating OXPHOS in SCNCs could unveil new insights into SCNC biology. To explore the influence
95 of mitochondrial function on SCNC development, we focused on peroxisome proliferator-activated
96 receptor gamma coactivator 1-alpha (PGC-1α)[51], a transcriptional co-activator widely recognized as a
97 potent regulator of mitochondrial biogenesis and OXPHOS. Originally identified for its role in cold-induced
98 adaptive thermogenesis through the regulation of OXPHOS genes[52], PGC-1α has since been implicated
99 in metabolic reprogramming during cancer development, demonstrating robust but varied effects across
100 cancer types[53]. In prostate cancer, it has been found to support the growth of localized, androgen-
101 dependent tumors[54,55] while restraining the progression of androgen-independent, metastatic forms[56–58].
102 In melanoma, PGC-1α is associated with tumors that exhibit enhanced mitochondrial function[59] and a
103 reduced metastatic potential[60]. It suppresses metastasis in non-small cell lung cancer (NSCLC)[61], but
104 promotes metastasis in other cancer models[62]. The specific impact of PGC-1α on SCNC has yet to be
105 determined.

106 To investigate the role of PGC-1α in regulating SCNC development, we performed an integrated
107 computational and functional investigation. Bioinformatics analyses of 10,529 patient tumors and 1,466
108 human cancer cell lines were performed, followed by functional and mechanistic analyses using a human
109 prostate tissue-derived SCN transformation system, referred to as PARCB[2,3,13]. This system enables the
110 transformation of normal human lung epithelial cells, prostate epithelial cells, or bladder urothelial cells
111 into SCNC via transduction with an oncogene cocktail abbreviated as PARCB (TP53DN, myr-AKT,
112 shRB1, c-MYC, and BCL2). This model generates two distinct tumor lineages characterized by either
113 stem-like (POU2F3/ASCL2 subtype) or neuroendocrine features (ASCL1 subtype) that closely resemble
114 the POU2F3 and ASCL1 subtypes seen in clinical SCNCs[13]. Here, we reveal the metabolic heterogeneity
115 between SCNC subtypes and identify PGC-1α as a driver of the ASCL1 lineage.

116

117 **RESULTS**

118 Elevated PGC-1α in clinical SCNC correlates with increased ASCL1 expression and neuroendocrine
119 differentiation.

120 To investigate the role of PGC-1α in SCNCs, we conducted bioinformatics analyses in a wide
121 range of human cancer cell lines, human primary tumors, and clinical SCN datasets. First, a co-
122 expression analysis was conducted on PGC-1α against the four SCNC lineage markers—ASCL1,
123 POU2F3, NEUROD1, and YAP1—across all 1,466 human cancer cell lines from the Cancer Cell Line
124 Encyclopedia (CCLE). PGC-1α shows no correlation with POU2F3, NEUROD1, or YAP1 (**Figure S1A**).
125 Conversely, PGC-1α exhibits a positive correlation with ASCL1, a pioneer transcription factor that is
126 essential for neuronal commitment and SCNC progression[63–65]. Notably, a subpopulation of cell lines with
127 high ASCL1 expression has a co-upregulation of PGC-1α (**Figure 1A**). This subpopulation is comprised
128 predominantly of two neuroendocrine cancer cell types: small cell lung cancer (SCLC) and
129 neuroblastoma (34/43, 79%) (**Figure 1A**). Consistently, PGC-1α expression is elevated in SCLC and
130 neuroblastoma cell lines compared with NSCLC (**Figure S1B**). To check whether the subpopulation of
131 cells with PGC-1α/ASCL1-High expression have increased SCN differentiation, we applied a well-
132 established SCN score derived from a pan-cancer transcriptomic analysis[1]. A higher SCN score indicates
133 a more SCN-like phenotype (see Methods section for more details). Cell lines with high PGC-1α and
134 ASCL1 expression have a higher SCN score compared with the rest of the samples, indicating
135 heightened neuroendocrine differentiation (**Figure 1B**). Together, these data suggest a link between
136 PGC-1α, ASCL1, and SCN differentiation.

137 To check whether PGC-1α expression correlates with ASCL1 and SCN differentiation in patient
138 tumors, we analyzed 10,529 solid tumors from The Cancer Genome Atlas (TCGA)[66]. Consistent with the
139 CCLE cancer cell lines, a subpopulation of patient tumors has elevations in both PGC-1α and ASCL1
140 expression (**Figure S1C**), and a higher SCN score (**Figure 1C**). Next, the analysis was extended to
141 include clinical SCN samples. Clinical datasets were mined from multiple cancers, including clinical lung
142 adenocarcinoma (LUAD), castration resistant prostate cancer (CRPC), SCN prostate cancer (NEPC),
143 and SCLC. As in the human cancer cell lines (from the CCLE) and patient tumors (from the TCGA), the

144 majority of clinical samples with increased ASCL1 expression have high PGC-1α expression (**Figure**
145 **1D)**. Most patient samples with high PGC-1α and ASCL1 expression (56/83; 67%) in this dataset were
146 neuroendocrine cancers and have a higher SCN score (**Figure 1D, right panel**). Consistent with these
147 observations, PGC-1α expression is increased in SCN prostate cancer compared with castration
148 resistant prostate cancer (CRPC)[67] and in SCLC[68] compared with NSCLC[66] (**Figure 1E**). Of note, the
149 increased PGC-1α expression in SCLC is largely attributable to a neuroendocrine subtype expressing
150 ASCL1 (SCLC-A), further corroborating the link between PGC-1α and ASCL1 (**Figure 1E, right panel**).
151 Epithelial ovarian cancers, particularly high-grade serous ovarian carcinomas (HGSOC), share
152 genomic alterations with neuroendocrine tumors including mutations in TP53, loss of RB1, and
153 amplification of MYC[69]. We therefore examined expression of PGC-1α and its correlation with ASCL1 in
154 a cohort of patients with a diagnosis of HGSOC. A positive correlation between PGC-1α and ASCL1 is
155 also observed in these samples (**Figure S1D**), highlighting a consistent link across multiple clinical
156 sample types.
157 Given the contribution of ADT to SCN prostate cancer progression[5,6], we next examined the effect
158 of ADT on the PGC-1α expression in prostate cancer (**Figure 1F**). A clinical transcriptomic dataset was
159 utilized in which tumors were biopsied from the same prostate cancer patients before and after ADT with
160 enzalutamide, a potent and selective antagonist of the androgen receptor[70]. ADT-treated tumors exhibit
161 increased PGC-1α expression, which is positively correlated with ASCL1 (**Figure 1F**). To identify
162 enriched pathways upon ADT treatment, we performed gene set enrichment analysis (GSEA) on patient
163 samples before and after ADT. This analysis revealed OXPHOS as a top enriched pathway in post-ADT
164 tumors (**Figure 1G**). As expected, the Androgen Response pathway is a top downregulated pathway in
165 patient tumors post-ADT (**Figure 1G**). Collectively, these data indicate that PGC-1α expression is
166 upregulated in multiple SCNC types and uncover a link between PGC-1α, ASCL1, and SCN
167 differentiation.
168
169 <u>Enhanced PGC-1α expression and OXPHOS activity in SCN prostate cancer within the ASCL1 tumor</u>
170 <u>subtype.</u>

171 Having established a link between PGC-1α and ASCL1 in multiple clinical SCNCs, we next sought
172 to investigate the functional role of PGC-1α in specific SCNCs subtypes. With this goal in mind, we utilized
173 our human tissue-derived PARCB-induced SCN transformation model[13]. This model produces ASCL1
174 and POU2F3/ASCL2 subtypes, closely resembling clinical SCLC and SCN prostate cancer subtypes
175 (**Figure 2A**). To determine if PGC-1α is linked to the ASCL1 subtype in the PARCB model, we conducted
176 a co-expression analysis across all PARCB time course samples. This analysis revealed a tight and
177 positive correlation between PGC-1α and ASCL1, exclusively observing the highest expression of both
178 genes in the ASCL1 subtype (**Figure 2B**). Corroborating this observation, PGC-1α expression markedly
179 increased in five out of ten PARCB tumor series derived from distinct donor tissue series (**Figure 2C**).
180 Moreover, across all the patient series, the ASCL1 neuroendocrine subtype demonstrated a 16-fold
181 higher expression of PGC-1α compared with the POU2F3/ASCL2 subtype (**Figure 2D)**. To check
182 whether PGC-1α and ASCL1 are co-expressed at the single cell level, we examined single-cell RNA-
183 sequencing (scRNA-seq) from the same PARCB time course dataset[13]. The analysis revealed that high
184 PGC-1α expression was almost exclusively associated with ASCL1, while it was absent in cells
185 expressing POU2F3 or ASCL2 (**Figure S2**). Collectively, these data indicate increased PGC-1α
186 expression in the PARCB model's ASCL1 subtype, which aligns with the bioinformatics analyses in
187 patient tumors and clinical datasets described in Figure 1.

188 Building on our findings that PGC-1α expression is elevated in the ASCL1 tumor subtype, we
189 further investigated the regulatory mechanisms underlying this phenomenon. Specifically, we aimed to
190 determine if transcription factors (TFs) co-activated by PGC-1α are more accessible in the ASCL1
191 subtype than in the POU2F3/ASCL2 subtype. To this end, we employed Hypergeometric Optimization of
192 Motif EnRichment (HOMER) analysis was performed to compare the accessible peaks in both tumor
193 subtypes. There was a notable enrichment of TFs co-activated by PGC-1α in the ASCL1 tumor subtype,
194 several of which were among the most significantly enriched (**Figure 2E**). This enrichment suggests
195 enhanced PGC-1α-induced TF signaling in the ASCL1 subtype.

196 To define the transcriptional changes associated with the development of the ASCL1 subtype in
197 an unbiased manner, GSEA was performed in tumors of the ASCL1 subtype versus all the other stages

198 of PARCB transformation (**Figure 2F**). Consistent with their high PGC-1α expression and TF signaling,
199 ASCL1 tumors had pronounced upregulation of oxidative phosphorylation (OXPHOS) genes (**Figure 2F**),
200 indicating increased mitochondrial biogenesis and/or activity. To determine whether the increased
201 OXPHOS expression translated to higher OXPHOS activity, we performed Seahorse respirometry. This
202 plate-based extracellular flux analysis utilizes multiple inhibitors targeting different components of the
203 OXPHOS machinery, providing a detailed functional profile of OXPHOS activity[71]. Seahorse respirometry
204 revealed that PARCB-ASCL1 tumor-derived cell lines exhibited a marked increase in basal and maximal
205 oxygen consumption rates compared with the POU2F3/ASCL2 subtype (**Figure 2G**), indicating increased
206 OXPHOS activity. Furthermore, the ASCL1 tumor subtype had higher expression of both subunits of the
207 mitochondrial pyruvate carrier (MPC) (**Figure 2H**), an obligate heterodimer in the mitochondrial inner
208 membrane that allows entry of pyruvate into the mitochondrion[72]. These findings demonstrate that the
209 ASCL1 subtype exhibits enhanced PGC-1α expression and OXPHOS activity.
210
211 <u>PGC-1α inhibition blunts OXPHOS, reduces the growth of SCNC cell lines, and blocks SCN prostate</u>
212 <u>tumor formation.</u>
213 Considering the high PGC-1α expression and high OXPHOS activity in the PARCB ASCL1
214 subtype described in Figure 2, we next asked whether PGC-1α is important for PARCB tumor
215 progression. To investigate, PGC-1α was inhibited during PARCB prostate transformation using shRNA
216 interference (**Figure 3A**). PGC-1α inhibition was verified using RT-qPCR in PARCB organoids before
217 xenografting into immunocompromised mice for tumor formation (**Figure 3B**). Strikingly, PGC-1α
218 inhibition blocked PARCB tumor growth, underscoring its requirement for PARCB prostate tumor
219 initiation.
220 Since PARCB tumors could not form under PGC-1α inhibition, we explored its role in maintaining
221 PARCB-derived ASCL1 and POU2F3/ASCL2 prostate cancer cell lines. PGC-1α inhibition reduced the
222 proliferation of both subtypes and the response was unexpectedly more pronounced in the POU2F3
223 subtype (**Figures 3C and 3D**). Next, we examined whether pharmacological inhibition of PGC-1α
224 similarly affects cell proliferation. Post-translational modifications are recognized as key regulators of

225 PGC-1α activity[73,74]. Among these, acetylation of lysine residues is one of the most well-characterized
226 modifications impacting PGC-1α activity. A recent high-throughput screen identified a small molecule
227 inhibitor called SR-18292 that increases PGC-1α lysine acetylation and inhibits PGC-1α activity by
228 blocking its interaction with HNF4A[75]. As with genetic inhibition, SR-18292 treatment suppressed growth
229 in both ASCL1 and POU2F3/ASCL2 subtypes, with a stronger effect on the POU2F3ASCL2 subtype
230 (**Figure S3**).

231 To determine whether the effect of PGC-1α inhibition extends beyond the PARCB-derived cell
232 lines, we tested patient-derived SCN prostate and lung cancer cell lines. PGC-1α inhibition reduced the
233 growth of the sole patient-derived SCN prostate cancer cell line, NCI-H660 (**Figure 3E**). Similarly,
234 analysis of PGC-1α inhibition in the Cancer Dependency Map (DepMap)[76] revealed a stronger anti-
235 proliferative effect in SCLC compared with NSCLC (**Figure 3F**). Taken together, these findings indicate
236 that PGC-1α inhibition blunts the growth of multiple SCNC types.

237 We next sought to understand the functional mechanism behind PGC-1α inhibition's impact on
238 SCNC cell line growth and PARCB tumor suppression. Accordingly, we inhibited PGC-1α in ASCL1 and
239 POU2F3/ASCL2 cell lines using shRNA and performed Seahorse respirometry to examine the effect on
240 mitochondrial function. PGC-1α inhibition downregulated basal and maximal respiration in both the
241 ASCL1 and POU2F3/ASCL2 subtypes (**Figure 3G**), highlighting the importance of PGC-1α in maintaining
242 OXPHOS activity across both subtypes. These findings collectively suggest that PGC-1α is essential for
243 the initiation of PARCB prostate tumors and sustaining OXPHOS and proliferation of cultured SCNC cell
244 lines.

245

246 <u>OXPHOS inhibition blunts SCN prostate and lung cancer cell line proliferation.</u>

247 Because PGC-1α inhibition blunted OXPHOS and reduced the growth of multiple cultured SCNC
248 cell types, we next asked whether OXPHOS specifically is required for the growth of SCNC cell lines.
249 First, PARCB cell lines derived from the ASCL1 and POU2F3/ASCL2 tumor subtypes were treated with
250 IACS-010759, a clinical-grade respiratory chain complex I inhibitor. This treatment abolished OXPHOS
251 in cell lines derived from both subtypes (**Figure 4A**). To confirm the inhibitor's specificity and ensure that

252 the observed effects were directly due to complex I inhibition, NDI1, a yeast complex I[48,77] was
253 overexpressed concurrently with complex I inhibition**.** NDI1 overexpressed fully rescued the OXPHOS
254 inhibition caused by IACS-010759 (**Figure 4A**). Interestingly, NDI1 overexpression boosted the oxygen
255 consumption rate (OCR) above baseline levels in the ASCL1 subtype (**Figure 4A**), suggesting that this
256 subtype not only has increased baseline levels of OXPHOS activity but may also have higher metabolic
257 plasticity.

258 Having verified that IACS-010759 blocks OXPHOS in these SCNC cell lines, we next asked
259 whether its treatment would reduce their proliferation in culture. In line with PGC-1α inhibition experiments
260 described in Figure 3, IACS-010759 treatment reduced proliferation of cell lines derived from both
261 subtypes, with a more pronounced effect in the POU2F3/ASCL2 subtype. These anti-proliferation effects
262 caused by IACS-010759 were fully rescued by NDI1 overexpression (**Figure 4B**), indicating high
263 specificity of the inhibitor. Given IACS-010759's specific action on respiratory chain complex I, we
264 pursued an additional method to inhibit OXPHOS in SCNC cell lines. We utilized IMT1B, a recently
265 developed small molecule inhibitor of mitochondrial RNA polymerase (POLRMT), which blocks
266 mitochondrial DNA transcription thereby downregulating all of the mitochondrially-encoded respiratory
267 chain complexes[78]. Mirroring our findings with IACS-010759, IMT1B treatment more potently affected the
268 POU2F3/ASCL2 subtype than the ASCL1 subtype (**Figure 4C**).

269 To extend our investigation of OXPHOS inhibition to other SCNC types, we examined the genetic
270 dependencies of 104 lung cancer cell lines in the DepMap database. We first performed unsupervised
271 principal component analysis (PCA) using the DepMap dependency scores. There was a distinct
272 separation between SCLC and NSCLC samples (**Figure 4D**), indicating unique genetic dependencies
273 between the two groups. Pathway enrichment analysis from the top and bottom 100 PC1 loading genes
274 indicated that OXPHOS is a top enriched pathway in SCLC versus NSCLC cancer cell lines, implying
275 that OXPHOS gene deletion has a stronger anti-proliferation effect in SCLC versus NSCLC (**Figure 4D**).
276 Collectively, these findings indicate that OXPHOS, like PGC-1α, is necessary for the maintenance of
277 SCNC cell lines, especially of the POU2F3/ASCL2 subtype.

278

279 PGC-1α overexpression promotes OXPHOS in the prostate cancer ASCL1 subtype.

280 As described above, PGC-1α inhibition reduced OXPHOS activity in SCNC cell lines. We
281 therefore asked whether PGC-1α overexpression is sufficient to promote OXPHOS, and whether this
282 metabolic shift would promote lineage plasticity. We first verified the PGC-1α overexpression construct
283 using western blot analysis in a panel of PARCB prostate cancer cell lines generated previously[2]. As
284 expected, PGC-1α overexpression increased both PGC-1α and OXPHOS protein levels (**Figure S4A**).
285 Next, PGC-1α was overexpressed in POU2F3/ASCL2 and ASCL1 PARCB tumor-derived cell lines, and
286 its effect on OXPHOS activity and neuroendocrine differentiation were measured. This analysis utilized
287 Seahorse respirometry, in vivo micro PET and computed tomography (microPET/CT) in vivo imaging,
288 and histology **(Figure 5A)**. PGC-1α overexpression upregulated OXPHOS activity in cells of the ASCL1
289 but not POU2F3/ASCL2 subtype (**Figure 5B**). This result is consistent with the ASCL1 subtype's selective
290 OXPHOS enhancement from yeast Complex I overexpression seen in Figure 4A, suggesting a relatively
291 fixed metabolic state in the POU2F3/ASCL2 subtype.

292 To check whether the increased OXPHOS caused by PGC-1α overexpression in cell lines would
293 translate to higher bioenergetics and SCN differentiation in tumors, ASCL1 or POU2F3/ASCL2 cell lines
294 with and without PGC-1α overexpression were xenografted into immunocompromised mice for tumor
295 initiation and subsequent microPET/CT imaging. PGC-1α overexpression promoted tumor growth only in
296 the ASCL1 subtype, but this effect did not reach statistical significance (**Figure 5C**). Although the effects
297 did not reach statistical significance, the increased tumor growth in the ASCL1 subtype was accompanied
298 by increased ^{18}F-FDG uptake (**Figure 5D**) and ^{18}F-BnTP[79] uptake in vivo (**Figure 5E**), indicating
299 heightened glucose uptake and mitochondrial content and/or activity, respectively.

300 We next checked whether tumors derived from ASCL2/POU2F3 or ASCL1 cell lines with PGC-
301 1α overexpression had increased SCN differentiation. We performed histological analysis from tumors
302 derived from both subtypes. There were no obvious histological changes in SCN differentiation upon
303 PGC-1α overexpression in either subtype (**Figure S4B**). Collectively, the data suggest that compared
304 with the ASCL1 subtype, the POU2F3/ASCL2 subtype exhibits a relatively fixed metabolic state, showing
305 a limited OXPHOS response to PGC-1α and NDI1 overexpression. Moreover, the data indicate that

306 despite the ASCL1 subtype's greater OXPHOS response to PGC-1α overexpression, PGC-1α alone is
307 not sufficient to trigger additional neuroendocrine differentiation in these terminally differentiated cell
308 lines.
309
310 PGC-1α overexpression upregulates OXPHOS and drives SCN prostate cancer towards an ASCL1-
311 expressing lineage.
312 In Figure 5 we showed that PGC-1α overexpression was not sufficient to induce lineage plasticity
313 of POU2F3/ASCL2 cells towards ASCL1, nor was it sufficient to induce further neuroendocrine
314 differentiation in terminally differentiated ASCL1 cells. We therefore asked whether PGC-1α
315 overexpression could promote SCN progression during PARCB transformation when the PARCB
316 oncogenes are actively restructuring the chromatin landscape to alter global gene expression. For this,
317 we conducted PARCB prostate transformation experiments with PGC-1α overexpression or control
318 constructs linked with BFP reporters, into the PARCB oncogene cocktail. (**Figure 6A**). PGC-1α
319 overexpression resulted in an approximate 100-fold increase in PGC-1α mRNA levels in PARCB prostate
320 organoids (**Figure S5A**) and a threefold higher tumor take rate compared with controls. (**Figure 6B**). The
321 majority of PGC-1α overexpressing tumors maintained high BFP expression months after transduction,
322 suggesting forward selection during transformation (**Figure S5B**). Consistently, PGC-1α protein levels
323 were higher in PGC-1α overexpressing tumors compared with control (**Figure S5C**). These data indicate
324 that PGC-1α overexpression promotes PARCB-induced SCN prostate tumor formation.
325 To better understand how PGC-1α overexpression promotes PARCB transformation, we
326 performed bulk RNA sequencing on PARCB tumors with PGC-1α overexpression and control. GSEA
327 revealed that PGC-1α overexpression in PARCB tumors upregulated OXPHOS gene expression (**Figure**
328 **6C**). Next, a detailed GSEA squared analysis was performed, ranking OXPHOS-related gene sets by
329 NES scores across multiple gene set families comprised over 10,000 gene sets (**Figure 6D**). This
330 analysis showed that OXPHOS gene sets were highly and exclusively enriched in PARCB tumors with
331 PGC-1α overexpression compared with control (**Figure 6D**). Thus, PGC-1α overexpression robustly
332 increases OXPHOS gene expression. Additionally, we explored adhesion-related pathways, known to be

333 broadly downregulated as cancers transition to a more SCN phenotype[1]. We observed a downregulation
334 of adhesion pathways in PARCB tumors that overexpressed PGC-1α, relative to the control group
335 (**Figure 6D**). These finding suggests that PGC-1α overexpression may promote SCN differentiation by
336 upregulating OXPHOS.

337 To quantify the effect of PGC-1α overexpression on SCN differentiation, we first categorized
338 tumors into PGC-1α-High and PGC-1α-Low groups, based on PGC-1α mRNA levels achieved by
339 overexpression. PGC-1α-high samples exhibited a higher SCN score (defined above, in the methods
340 section, and in reference[1]) compared with PGC-1α-low (**Figure 6E**). We also calculated SCN scores for
341 all 55 samples from our recently published PARCB time course study[13]. Notably, PGC-1α-high samples
342 not only displayed increased SCN differentiation in comparison to the PGC-1α-low samples from this
343 study, but also exhibited higher SCN scores than all samples from the temporal study (**Figure 6E**). To
344 determine whether these transcriptomic changes were mirrored at the protein level, we performed
345 immunohistochemistry in PARCB tumors sections with PGC-1α overexpression or control. Consistent
346 with the transcriptomic results in Figures 6C-6E, increased mitochondrial content (TOMM20) and
347 neuroendocrine (NCAM1) expression were observed in PGC-1α-High tumor sections compared with
348 PGC-1α-Low (**Figure 6F**). These results indicate that high levels of PGC-1α overexpression upregulate
349 OXPHOS expression and promote SCN differentiation.

350 Building on the established relationship between PGC-1α and ASCL1 described above, we
351 investigated if PGC-1α overexpression could promote lineage plasticity towards the ASCL1 subtype. By
352 conducting a gene expression analysis on PARCB tumors categorized by high versus low PGC-1α
353 expression and analyzing signature genes of both ASCL1 and POU2F3/ASCL2 subtypes, we detected a
354 distinct expression pattern. Notably, PGC-1α-high samples predominantly expressed genes associated
355 with the ASCL1 subtype, whereas PGC-1α-low samples exhibited an increased expression of
356 POU2F3/ASCL2 subtype genes (**Figure 6G**). This pattern underscores PGC-1α's potential influence in
357 steering lineage specificity towards ASCL1.

358 To determine if these expression patterns are observable in a broader clinical context, our
359 datasets from PARCB tumors with PGC-1α overexpression were projected onto datasets from SCLC

360 samples in the CCLE and from the clinical study by George et al. 2015[68] (**Figure 6H**). We also included
361 the ASCL1 and POU2F3/ASCL2 PARCB samples from our recently published study[13]. PGC-1α-high
362 samples clustered well with SCLC-ASCL1 and PARCB-ASCL1 tumors (HC6), whereas PGC-1α-low
363 samples clustered better with SCLC-POU2F3 and PARCB-POU2F3/ASCL2 tumors (HC5). Collectively,
364 these data suggest that PGC-1α promotes SCNC progression towards an ASCL1-expressing subtype
365 with increased OXPHOS capacity.
366
367 ASCL1 overexpression upregulates PGC-1α expression
368 Considering the shared molecular alterations in cells of both ASCL1 and POU2F3/ASCL2
369 subtypes, we aimed to identify the transcription factor specifically driving PGC-1α expression in the
370 ASCL1 lineage. Given ASCL1's role as a pioneer transcriptional activator, we focused on whether ASCL1
371 itself can influence PGC-1α expression. To this end, we analyzed data from our prior study where ASCL1
372 was overexpressed in two PARCB POU2F3/ASCL2 tumor-derived cell lines, which do not express PGC-
373 1α[13] (**Figure 7A**). ASCL1 overexpression switched on the expression of PGC-1α in both cell lines (**Figure**
374 **7A**). These results indicate that ASCL1 itself can regulate PGC-1α expression.
375 To validate this regulatory role of ASCL1 in PGC-1α expression, we investigated a newly
376 developed in vitro model for SCN prostate cancer differentiation focusing on the androgen-insensitive
377 C4-2B cell line[80]. This model induces SCN differentiation in C4-2B cells by incorporating a specific set of
378 SCN oncogenes and transcription factors, namely PRNBSAN (dominant-negative TP53, shRB1, MYCN,
379 BCL2, SRRM4 combined with ASCL1, or NEUROD1) (**Figure 7B**). Consistent with the observations in
380 the PARCB models, we observed a tight expression correlation between PGC-1α and ASCL1 in this
381 model (**Figure 7C**). Moreover, ASCL1 overexpression (PRNBSA) elevated PGC-1α levels, which
382 correlated with enhanced SCN differentiation (**Figure 7D**). These findings establish ASCL1 as a positive
383 regulator of PGC-1α expression and reinforce the functional connection between PGC-1α, ASCL1, and
384 neuroendocrine differentiation.
385 To better understand how ASCL1 enhances PGC-1α expression, we explored its direct interaction
386 with gene promoters of PGC-1α. We analyzed ASCL1 ChIP-Seq datasets from SCN lung[81,82] and

387 prostate cancer cell lines[64,80], as well as in LuCaP prostate cancer patient-derived xenografts (PDXs)[12].
388 Our analysis indicated variable binding of ASCL1 to PGC-1α DNA, with inconsistent effects across
389 different studies and samples. Specifically, ASCL1's binding to an alternative promoter of PGC-1α,
390 particularly at exon 1b[74] encoding transcript variant X2 (XM_005248132.1), was modest in SCN lung and
391 prostate cancer cell lines but absent in prostate cancer PDX models (**Figures 7E and S6**). In contrast,
392 prostate cancer PDX models showed ASCL1 with a stronger affinity for variant 1 (NM_001330751.2) of
393 PGC-1α, a pattern not observed in SCN lung and prostate cancer cell lines (**Figure S7**). Additionally,
394 ASCL1's interaction within the PGC-1α gene body was exclusive to SCN lung cancer cell lines and was
395 not present in SCN prostate cancer cell lines and PDX models (**Figure S8**). The variable binding of
396 ASCL1 to PGC-1α DNA across datasets and model systems precludes definitive conclusions about
397 ASCL1's consistent interaction with the PGC-1α gene.
398
399 **DISCUSSION**
400 Metabolic heterogeneity and plasticity in SCNC subtypes
401 Our study sheds light on the role of mitochondrial metabolism on lineage plasticity in SCNCs. Our
402 findings reveal metabolic heterogeneity between the ASCL1 and POU2F3/ASCL2 SCNC subtypes,
403 distinguished by their respective PGC-1α expression and OXPHOS capacities. Specifically, the ASCL1
404 subtype has higher PGC-1α expression and OXPHOS activity compared with the POU2F3/ASCL2
405 subtype. Additionally, the ASCL1 subtype has increased metabolic flexibility as evidenced by its heighted
406 OXPHOS response to overexpression of both PGC-1α and NDI1, the respiratory chain complex I from
407 *Saccharomyces cerevisiae*. Conversely, the POU2F3/ASCL2 subtype has a more fixed metabolic state,
408 showing no OXPHOS response to the same genetic perturbations. Moreover, using genetic PGC-1α
409 gain-of-function during PARCB-induced SCN prostate transformation, we discovered that PGC-1α
410 triggers a metabolic shift towards OXPHOS and promotes differentiation towards an ASCL1-expressing
411 SCN prostate cancer subtype.
412
413 The role of PGC-1α and OXPHOS during androgen deprivation therapy

414 Recent studies indicate increased reliance of prostate cancer cells on OXPHOS after androgen
415 deprivation therapy (ADT)[83,84]. Consistently, our analysis of a clinical dataset in which tumors were
416 sampled from prostate cancer patients before and after ADT using enzalutamide[70] indicated that post-
417 treatment tumors had increased PGC-1α expression. Furthermore, OXPHOS was a top enriched
418 pathway upon ADT. These observations suggest that ADT may induce a strong selection pressure on
419 prostate cancer cells to increase their reliance on OXPHOS, thereby facilitating progression to the SCN
420 state. Thus, targeting the PGC-1α-OXPHOS axis during and after ADT may have a powerful therapeutic
421 effect against SCN prostate cancer progression.
422
423 Targeting the PGC-1α-OXPHOS axis in SCNCs
424 Although both subtypes were sensitive to PGC-1α and OXPHOS inhibition, the bioenergetically
425 quieter POU2F3/ASCL2 subtype was more sensitive to both perturbations than the ASCL1 subtype. The
426 heightened sensitivity of the POU2F3/ASCL2 subtype may be attributable to two characteristics: 1) its
427 lower levels of PGC-1α and OXPHOS activity, which makes it easier to reduce their levels, and/or 2) its
428 reduced metabolic flexibility, making it unable to shift its metabolic state to tolerate the OXPHOS
429 inhibition. Our characterization of the subtype-specific metabolic vulnerabilities within SCNCs may inform
430 therapeutic strategies.
431 In light of the intimate relationship between mitochondrial metabolism and cancer, OXPHOS
432 inhibitors are being actively explored as potential cancer treatments[47–49]. IACS-010759, a potent and
433 selective respiratory chain complex I inhibitor recently explored in clinical trials[47,85–87], can potentially be
434 repurposed to target SCNCs. Despite these initial trials being halted due to peripheral neurotoxicity and
435 lactic acidosis[88] (on target, off tumor toxicities), SCNCs of the POU2F3/ASCL2 subtype may demonstrate
436 a broader therapeutic window for this drug because of their increased reliance on OXPHOS. Notably,
437 IACS-010759 showed a partial response and alleviation of cancer-related pain in a patient with castration-
438 resistant prostate cancer[85,89]. However, the neuroendocrine differentiation status of the patient's cancer
439 is unknown.Targeting PGC-1α could be another approach to controlling SCNC progression. Although
440 direct inhibitors of PGC-1α are not currently available, there are several small-molecule inhibitors that

441 can regulate PGC-1α related pathways[73]. Most of these small molecules have been designed to activate
442 its expression. However, recent studies have also identified small molecules that can inhibit PGC-1α.
443 One such molecule is SR-18292[75], which increased PGC-1α lysine acetylation in hepatocytes by blocking
444 its interaction with the histone acetyltransferase KAT2A (GCN5), reducing genes involved in
445 gluconeogenesis[90,91]. In our study, PGC-1α inhibition with SR-18292 reduced the proliferation of PARCB-
446 tumor derived cell lines, with a more pronounced effect in the POU2F3/ASCL2 subtype. While this
447 inhibitor was reported to diminish OXPHOS activity[92], its PGC-1α-related roles beyond OXPHOS in
448 SCNCs warrants further investigation. Future research should also investigate the metabolic
449 vulnerabilities in the NEUROD1 and YAP1 subtypes, which were not addressed in our study.
450
451 ASCL1's upstream regulation of PGC-1a initiates a potential positive feedback loop
452 Our investigation into the ASCL1-PGC-1α interaction encompassed comprehensive
453 bioinformatics analyses of thousands of patient tumors, human cancer cell lines, and multiple clinical
454 SCNC datasets, along with functional experiments in SCNC models PARCB and PRNBSAN. These
455 efforts demonstrated a strong correlation between PGC-1α and increased ASCL1 expression.
456 Exogenously elevating ASCL1 levels enhanced PGC-1α expression, indicating that ASCL1 may be an
457 upstream activator of PGC-1α. Moreover, the PGC-1α overexpression experiments depicted in Figure 6
458 demonstrate that enhancing PGC-1α during PARCB transformation promotes lineage plasticity towards
459 the ASCL1 subtype. Together, these observations point to a potential positive feedback mechanism
460 where ASCL1 elevates PGC-1α levels, which in turn, further increases ASCL1 expression, thereby
461 intensifying PGC-1α's effect and encouraging lineage plasticity towards the ASCL1 subtype.
462 While analysis of existing ASCL1 ChIP-Seq datasets revealed some evidence of ASCL1 binding
463 to PGC-1α's promoters and gene body, hinting at a direct regulatory mechanism, inconsistencies across
464 datasets—likely due to differences in experimental sample types and the ASCL1 antibodies used—
465 render the direct binding role of ASCL1 to PGC-1α inconclusive. Thus further research is needed to
466 elucidate the precise interaction between PGC-1α and ASCL1, including the exploration of indirect
467 pathways by which ASCL1 may modulate PGC-1α levels. Future research should also investigate

468 whether PGC-1α can directly bind to ASCL1 to co-activate it. Considering the significant influence of the
469 tumor microenvironment on cancer progression[93], future studies should also investigate how external
470 microenvironmental factors may initiate or influence the genetic interaction between PGC-1α and ASCL1.
471
472 Concluding remarks
473 We identify PGC-1α as a driver of SCN prostate cancer, promoting lineage plasticity towards an
474 ASCL1-expressing subtype. Moreover, our findings reveal that the POU2F3/ASCL2 subtype
475 demonstrates an increased sensitivity to PGC-1α and OXPHOS inhibition, attributable to its distinct
476 metabolic profile. Specifically, it has relatively low levels of PGC-1α and OXPHOS, coupled with a
477 relatively fixed metabolic state compared to the ASCL1 subtype. These characteristics likely underpin
478 the POU2F3 subtype's vulnerability to inhibition of PGC-1α and OXPHOS. Collectively, these observation
479 suggests the need for tailored treatment strategies that account for each tumor subtype's unique
480 metabolic makeup. As research continues to unravel the intricate relationship between metabolic
481 reprogramming and SCNC progression, our findings should aid in developing more effective therapies
482 for these notoriously resistant cancers.
483
484 **ACKNOWLEDGEMENTS**
485 We thank the University of California, Los Angeles (UCLA) Tissue Procurement Core Laboratories for
486 prostate tissue preparation and histological staining, and the UCLA Technology Center for Genomics and
487 Bioinformatics for RNA sequencing. We thank Nicholas Bayley at UCLA for RNA-sequencing data
488 processing. The microPET/CT imaging in this study was supported by the NIH Cancer Center Support
489 Grant (2 P30 CA016042-44). The GNEXT PET/CT scanner was funded by NIH S10 Shared
490 Instrumentation for Animal Research Grant (1 S10 OD026917-01A1). We thank Linsey Stiles and Katrina
491 P. Montales of the UCLA Mitochondria and Metabolism Core for assistance with the XF96 Extracellular
492 Flux Analyzer. We thank the following UCLA undergraduate research assistants who helped with wet lab
493 experiments: Spencer Gaut, Alitzel Martinez, Michelle Garcia, and Kathy Rivera.

Funding: The G. Harold and Leila Y. Mathers Charitable Foundation (O.N.W.). NIH UCLA SPORE in Prostate Cancer Grant P50CA092131 (O.N.W. and T.G.G.). NIH R01 Grant R01CA222877 (O.N.W. and T.G.G.), W. M. Keck Foundation Award 20182490 (O.N.W. and T.G.G.), UCLA Eli and Edythe Broad Center of Regenerative Medicine and Stem Cell Research Hal Gaba Director's Fund for Cancer Stem Cell Research (O.N.W. and T.G.G.). G.V. was supported by a Tumor Cell Biology Training Program NIH Grant (NIH T32 CA-009056). SM and GAD are partially supported by Veteran Affairs funds I01BX006019 and I01BX004651 to SM. SM and GAD are also supported by UCLA Eli and Edythe Broad Center of Regenerative Medicine and Stem Cell Research Award, supported by the Binder Foundation to SM and TG. F.N.E. was supported by a University of California–Historically Black Colleges and Universities (UC–HBCU) Initiative Fellowship provided by University of California Office of the President (UCOP).

AUTHOR CONTRIBUTIONS

Conceptualization: G.V., O.N.W.; Methodology: G.V., S.X., J.W.P., T.G., O.N.W.; Formal Analysis: G.V., C.C., J.F., T.H., W.T., K.S., F.N.E., L.W.; Investigation: G.V., D.C., F.N.E., G.A.B.; Resources: C.C., J.W.P., S.M.; Writing: Original Draft Preparation: G.V.; Writing: G.V., E.A., O.N.W.; Visualization: G.V.; Supervision: S.M., T.G., O.S., O.N.W.

DECLARATION OF INTERESTS

O.N.W. currently has consulting, equity, and/or board relationships with Trethera Corporation, Kronos Biosciences, Sofie Biosciences, Breakthrough Properties, Vida Ventures, Nammi Therapeutics, Two River, Iconovir, Appia BioSciences, Neogene Therapeutics, 76Bio, and Allogene Therapeutics. T.G.G. reports having consulting and equity agreements with Auron Therapeutics, Boundless Bio, Coherus BioSciences and Trethera Corporation. None of these companies contributed to or directed any of the research reported in this article.

MAIN FIGURE LEGENDS

520 **Figure 1.** Elevated PGC-1α in clinical SCNC correlates with increased ASCL1 expression and
521 neuroendocrine differentiation.

522 A. Gene expression analysis across all human cancer cell lines from the Cancer Cell Line
523 Encyclopedia (CCLE). Left panel: co-expression analysis between PGC-1α and ASCL1,
524 highlighting samples with high expression levels of both genes (boxed region). Right panel: pie
525 charts illustrating the proportion of cancer types exhibiting elevated co-expression of PGC-1α and
526 ASCL1, in contrast to the rest of the samples. See also Figure S1A.

527 B. Related to Figure 1A: Transcriptomic examination of small cell neuroendocrine (SCN)
528 differentiation in CCLE human cancer cell lines. SCN scores (defined previously[3] and detailed in
529 the Methods) are calculated for cells showing heightened PGC-1α and ASCL1 expression versus
530 the rest of the cells.

531 C. Related to Figure S1C: A transcriptomic analysis of SCN differentiation in all the patient tumors
532 from the TCGA database shown in Figure S1C. SCN scores are calculated from the boxed tumor
533 samples with elevated PGC-1α and ASCL1 expression compared with the rest of the samples.

534 D. Gene expression analysis in multiple clinical SCNC datasets[67,68,94–97]. Left panel: co-expression
535 analysis of PGC-1α and ASCL1. Right panel: SCN scores of the boxed samples with elevated
536 PGC-1α and ASCL1 expression compared with the rest of the samples.

537 E. PGC-1α expression levels in multiple SCNC datasets. SCLC subtypes are denoted as follows: P,
538 POU2F3; A, ASCL1; N, NEUROD1; Y, YAP1. The datasets used are indicated.

539 F. Transcriptomic analyses in clinical prostate cancer tumors before and after androgen deprivation
540 therapy (ADT) with enzalutamide. Left panel: a schematic overview. Middle panel: Comparison of
541 PGC-1α expression levels pre- and post-ADT. Right panel: Co-expression analysis of PGC-1α
542 and ASCL1 in (combined pre- and post-treatment analysis). See also Figure 1G.

543 G. Gene set enrichment analysis (GSEA) of differentially expressed genes in pre- versus post ADT-
544 treated tumors. See also Figure 1F.

545 Data for Figures 1B-1F are expressed as mean ± SEM, with significance denoted as **** ($p \leq 0.0001$),
546 ** ($p \leq 0.01$), and * ($p \leq 0.05$). The green lines represent the best-fit linear regression model, with the

547 indicated R^2 and p-values. All Log2 values have been upper quartile normalized with a pseudocount
548 of 1 (Log2 UQN+1). For statistical tests used, see Material and Methods section.
549
550 Related data can be found in Figure S1. Abbreviations: SCLC, small cell lung cancer; NEPC,
551 neuroendocrine prostate cancer; CRPC, castration resistant prostate cancer; LUAD, lung
552 adenocarcinoma.
553
554 **Figure 2.** Enhanced PGC-1α expression and OXPHOS activity in SCN prostate cancer within the ASCL1
555 tumor subtype.
556 A. Schematic illustrating PARCB-induced SCN prostate transformation, highlighting the bifurcation
557 of end stage tumors into the POU2F3/ASCL2 and ASCL1 lineages.
558 B. Co-expression analysis of PGC-1α and ASCL1 during PARCB prostate transformation. Note that
559 tumors with the highest expression levels of both genes are exclusively found in the ASCL1
560 subtype.
561 C. Analysis of PGC-1α expression levels during PARCB transformation in 5 out of 10 patient series
562 showcasing increased PGC-1α expression over time.
563 D. Comparative expression levels of PGC-1α in POU2F3/ASCL2 versus ASCL1 PARCB tumor
564 subtypes indicating subtype-specific expression patterns.
565 E. Hypergeometric Optimization of Motif EnRichment (HOMER) analysis across PARCB tumors
566 from both POU2F3/ASCL2 and ASCL1 subtypes. PGC-1α interacting transcription factors were
567 identified from the STRING database[98].
568 F. GSEA in the ASCL1 tumor subtype versus the rest of the PARCB time course samples. Gene
569 Ontology Biological Process (GOBP) gene sets were used. The pie chart indicates the proportion
570 of enriched gene sets related to mitochondrial OXPHOS.
571 G. Seahorse respirometry in PARCB tumor-derived cell lines from both the POU2F3/ASCL2 and
572 ASCL1 subtypes. Inhibitors used: Oligo, Oligomycin; FCCP, Carbonyl cyanide-p-
573 trifluoromethoxy-phenylhydrazone; Rot/AA, rotenone / antimycin A.

574 H. Expression of the mitochondrial pyruvate carrier in ASCL1 and POU2F3/ASCL2 PARCB tumor
575 subtypes.
576
577 All data, except in Figure 2G, utilizes data extracted from our recently published Chen et al. 2023
578 dataset[13]. The black line in Figure 2B represents the best-fit linear regression model, with the
579 indicated R^2 and p-values. Data in Figures 2D, 2G, and 2H are presented as mean ± SEM, with
580 significance levels marked as follows: **** ($p \leq 0.0001$), *** ($p \leq 0.001$), ** ($p \leq 0.01$), and * ($p \leq 0.05$). All
581 Log2 values are Log2 UQN+1. For statistical tests used, see Material and Methods section.
582
583 Related data can be found in Figure S2.
584
585 **Figure 3.** PGC-1α inhibition blunts OXPHOS, reduces the growth of SCNC cell lines, and blocks SCN
586 prostate tumor formation.
587 A. Schematic illustrating PARCB prostate transformation with PGC-1α knockdown.
588 B. PGC-1α mRNA levels using RT-qPCR in PARCB-transduced prostate organoids.
589 C. Cell proliferation analysis in ASCL1 tumor-derived cell lines from the PARCB model, comparing
590 PGC-1α knockdown (KD) cells to control. The blue fluorescence in the micrographs is derived
591 from the shPGC-1α and shControl constructs, which have co-linked expression of a blue
592 florescence protein (EBFP2).
593 D. Cell proliferation analysis in POU2F3/ASCL2 tumor-derived cell lines from the PARCB model with
594 PGC-1α KD versus control.
595 E. Cell proliferation analysis of a patient-derived SCN prostate cancer cell line (NCI-H660) with PGC-
596 1α KD compared with control.
597 F. PGC-1α inhibition (RNAi) effects on cell proliferation, represented by a dependency scores from
598 the DepMap database. a score of zero signifies no proliferation impact, negative values indicate
599 decreased proliferation, and a score of negative one corresponds to the median effect across all
600 pan-essential genes.

601 G. Seahorse respirometry in PARCB cell lines derived from the POU2F3/ASCL2 and ASCL1 tumor
602 subtypes. Oligo, Oligomycin; FCCP, Carbonyl cyanide-p-trifluoromethoxy-phenylhydrazone;
603 Rot/AA, rotenone / antimycin A.
604
605 Data in parts D, G, and H are presented as mean ± SEM, with significance levels marked as follows:
606 *** ($p \leq 0.001$), ** ($p \leq 0.01$), and * ($p \leq 0.05$). For statistical tests used, see Material and Methods section.
607
608 Related data can be found in Figure S3.
609
610 **Figure 4.** OXPHOS inhibition blunts SCN prostate and lung cancer cell line proliferation.
611 A. Seahorse respirometry in cell lines derived from the PARCB POU2F3/ASCL2 and -ASCL1 tumor
612 subtypes with the indicated conditions. Oligo, Oligomycin; FCCP, Carbonyl cyanide-p-
613 trifluoromethoxy-phenylhydrazone; Rot/AA, rotenone / antimycin A.
614 B. Cell proliferation analysis of cell lines derived from the POU2F3/ASCL2 and ASCL1 PARCB tumor
615 subtypes with the indicated treatments.
616 C. Cell proliferation analysis of cell lines derived from the PARC-POU2F3/ASCL2 and -ASCL1 tumor
617 subtypes treated with a mitochondrial DNA-directed RNA polymerase (POLRMT) inhibitor
618 (IMT1B) to block OXPHOS.
619 D. Analysis of differentially dependent genes in NSCLC and SCLC cell lines. Left panel:
620 unsupervised principal component analysis (PCA) on the genetic dependency data from all of the
621 lung cancer cell lines in the DepMap dataset. Right panel: normalized enrichment scores of gene
622 sets that separate PC1 low (SCLC) and PC1 high (NSCLC). The top 100 genes from the PC1
623 loading scores were used as input.
624 Data in Figure 4B are represented as mean ± SEM. with statistical significance denoted as ***
625 ($p \leq 0.001$) and ** ($p \leq 0.01$). For statistical tests used, see Material and Methods section.
626
627 **Figure 5.** PGC-1α overexpression promotes OXPHOS in the SCN prostate cancer ASCL1 subtype.

628 A. Left panel: overview of experimental strategy. Right panel: Details on the Positron Emission
629 Tomography (PET) probes utilized and their general mechanisms of action.
630 B. Seahorse respirometry in POU2F3/ASCL2 and ASCL1 PARCB tumor-derived cell lines. Oligo,
631 Oligomycin; FCCP, Carbonyl cyanide-p-trifluoromethoxy-phenylhydrazone; Rot/AA, rotenone /
632 antimycin A.
633 C. Caliper measurements of tumors initiated by subcutaneous injection of POU2F3/ASCL2 and
634 ASCL1 PARCB cell lines with PGC-1α overexpression versus control.
635 D. Left panel: overlay of in vivo micro PET and computed tomography (microPET/CT) scanning of a
636 mouse with a subcutaneous ASCL1 PARCB tumor imaged with ^{18}F-FDG indicting glucose uptake.
637 Right panel: quantification of ^{18}F-FDG uptake.
638 E. Left panel: microPET/CT of a mouse with a subcutaneous ASCL1 tumor imaged with ^{18}F-BnTP.
639 Right panel: quantification of ^{18}F-BnTP uptake indicating mitochondrial content. The inset has
640 been contrast enhanced to show the relatively low uptake of this probe in subcutaneous tumors,
641 as reported previously[99].
642
643 Data in Figure 5B are presented as mean ± SEM, with *** indicating a p-value ≤0.001. For statistical
644 tests used, see Material and Methods section. The absence of asterisks indicates that statistical
645 significance of p≤0.05 was not reached.
646
647 Related data can be found in Figure S4.
648
649 **Figure 6.** PGC-1α overexpression upregulates OXPHOS and drives SCN prostate cancer towards an
650 ASCL1-expressing lineage.
651 A. Schematic illustrating the experimental setup for assessing the effects of PGC-1α overexpression
652 versus a control vector on PARCB-induced prostate cancer transformation.
653 B. Comparison of the tumor establishment rate ("tumor take rate") between PARCB transformation
654 using PGC-1α overexpression compared with control. PARCB transformations were performed

655 using three separate patient donors, resulting in a total of 45 xenografts being implanted in 23
656 mice.

657 C. GSEA in PARCB tumors with PGC-1α overexpression versus control.

658 D. GSEA squared analysis depicting the distribution of normalized enrichment scores (NES) for
659 thousands of gene sets across multiple gene set families in samples with PGC-1α overexpression
660 versus control. See Materials and Methods section for details.

661 E. A transcriptomic analysis of SCN differentiation comparing SCN scores in PGC-1-High versus
662 PGC-1α-Low PARCB tumors. SCN scores calculated from datasets derived from Chen et al
663 2023[13] are also shown for comparison.

664 F. Immunohistochemistry in histological sections derived from PARCB tumors with high and low
665 levels of PGC-1α.

666 G. A heatmap displaying normalized gene expression levels for signature genes related to
667 POU2F3/ASCL2 and ASCL1 tumor subtypes in PGC-1α-High versus PGC-1α-Low tumors.

668 H. Principal Component Analysis (PCA) of PARCB samples, distinguishing between PGC-1α-High
669 and PGC-1α-Low PARCB tumors from this study, overlaid on PARCB tumors from our prior time
670 course study[13] and SCLC cell lines from the CCLE and George et al. 2015 clinical study[68].

671

672 Data in Figure 5E are presented as mean ± SEM, with statistical significance indicated by ****
673 ($p \leq 0.0001$) and *** ($p \leq 0.001$). For statistical tests used, see Material and Methods section.

674

675 Related data be can found in Figure S5.

676

677 **Figure 7.** ASCL1 overexpression upregulates PGC-1α expression

678 A. Expression levels of ASCL1 (left panel) and PGC-1α (right panel) after acute overexpression of
679 ASCL1 in cell lines derived from the PARCB POU2F3/ASCL2 tumor subtype. Data are mined
680 from Chen et al 2023[13]. Log2 values are Log2 UQN+1.

681 B. Schematic illustrating transformation of C42B cells to SCN prostate cancer using the PRNBSAN
682 oncogenes and transcription factors (dominant-negative TP53, shRB1, MYCN, BCL2, SRRM4,
683 ASCL1, and NEUROD1).
684 C. Co-expression analysis of PGC-1α and ASCL1 in C4-2B cells from the PRNBSAN transformation
685 system. Log2 values are Log2 FPKM+1.
686 D. Expression analysis of ASCL1 (top panel) and PGC-1α (bottom panel) from C4-2B cells
687 transduced with PRNBSAN. Log2 values are Log2 FPKM+1. The arrow indicates increased SCN
688 differentiation as observed Li et at. 2024[80].
689 E. ASCL1 ChIP Seq analysis in SCN prostate cancer and lung cancer cell lines from Li et al. 2024
690 and Augustyn et al. 2014. This gene locus represents Exon 1b, encoding transcript variant X2
691 (XM_005248132.1).
692
693 The data for Figure 7A and 7D are presented as mean ± SEM, with statistical significance denoted by **
694 ($p \leq 0.01$). For statistical tests used, see Material and Methods section.
695
696 Related data can be found in Figures S6-8.
697
698 **MATERIALS AND METHODS**
699 ***PARCB + PGC-1α transformation***
700 Donor prostate tissues were obtained in a de-identified manner and were therefore exempt from
701 Institutional Review Board (IRB) approval. The PARCB transformation assay was performed as
702 described previously[6] with modifications to the viral constructs to include PGC-1α gain- and loss-of-
703 function analyses. Briefly, donor prostate tissues were digested overnight and isolated cells were stained
704 to identify the basal cells. FACS sorted basal cells were combined with PARCB oncogene lentiviruses at
705 an MOI of 50 in Matrigel (Cat# 356234, Corning). The mixtures of basal cells, viral supernatant, and
706 Matrigel were plated in 48-well plates as hanging drop cultures until Matrigel solidified into domes. 20,000
707 basal cells were used per Matrigel dome, in a final volume of 20-30 µl per well. After Matrigel solidification,

708 organoids were cultured in prostate organoid media[78] at 37°C and 5% CO2 for 10-14 days. Transduced
709 organoids were harvested by dissociation of Matrigel with 1mg/mL Dispase (Cat# 17105041, Thermo
710 Fisher Scientific) and washed three times with PBS to remove Dispase. Washed organoids were re-
711 suspended in 10 µl of normal Matrigel and 10 µl Matrigel with high growth factors (Cat# 354248, Corning).
712 The organoid-Matrigel mixtures were implanted subcutaneously in immunodeficient NOD.Cg-Prkdcscid
713 Il2rgtm1Wjl/SzJ (NSG) mice[79] to initiate tumor formation. Tumors were extracted before ulceration or
714 reaching around 1 cm in diameter, whichever came first. NSG mice were obtained from the Jackson
715 Laboratories and housed and bred under the care of the Division of Laboratory Animal Medicine at the
716 University of California, Los Angeles (UCLA). All animal handling and subcutaneous injections were
717 performed following the protocols approved by UCLA's Animal Research Committee.
718
719 ***Cell lines and culture media***
720 The SCN prostate cancer line NCI-H660 (Cat# CRL-5813) was purchased from American Type Culture
721 Collection (ATCC). The PARCB-P3-TP5, PARCB-P2-TP6, and PARCB-P7-TP6 cell lines[13] and PARCB-
722 1, PARCB-11[2] cell lines were generated previously. All cells were maintained in stem cell culture media
723 (SCM): Advanced DMEM/F12 (Gibco CAT# 12634028), Glutamax (Gibco, CAT# 35050061), Pen/Strep,
724 B27 (Gibco CAT# 17504044), 10ng/ml human EGF (Peprotech CAT# 100-47, and 10ng/ml human FGF-
725 basic (Peprotech CAT# 100-18B). All cell lines were routinely tested for Mycoplasma using a MycoAlert™
726 PLUS Mycoplasma Detection Kit (Cat# LT07-703, Lonza).
727
728 ***Lentiviral vectors and high-titer lentivirus production***
729 The following three vectors for PARCB transformation were described previously: mristoylated AKT1
730 (FU-myrAKT1-CGW), c-MYC and BCL2 (FU-cMYC-P2A-BCL2-CRW), dominant negative TP53 (R175H)
731 and shRNA targeting of RB1 (FU-shRB1-TP53DN-CYW)[6]. For PGC-1α overexpression, a fourth vector
732 was designed. First, an FUGW backbone was subcloned to replace the EGFP with EBFP2 using Gibson
733 assembly (referred to as FUBW). Next, PGC-1α cDNA from pcDNA4 myc PGC-1 alpha (Addgene
734 #10974) was cloned into the FUBW backbone driven by a ubiquitin promoter. An empty FUBW backbone

735 without PGC-1α cDNA was used as a control. For PGC-1α inhibition during PARCB transformation,
736 shRNA targeting PGC-1α was cloned into the myristoylated AKT1 vector (FU-myrAKT1-CGW),
737 downstream of the H1 promoter. The following PGC-1α targeting sequence was used
738 TATGACAGCTACGAGGAATAT. As a control, a sequence that targets no known mammalian genes was
739 used (CAACAAGATGAAGAGCACCAA). For PGC-1α inhibition in cultured cell lines, the same shRNA
740 sequences were cloned into a pLKO_005 backbone, which was subcloned to replace its puromycin
741 resistance gene along with its promoter with CMV-EBFP2. High titer lentiviruses were made using a
742 previously established method[162].
743
744 ***Transduction of cultured SCN cell lines***
745 Cultured SCN cell lines, which grow in suspension as clusters, were mechanically dissociated using
746 gentle pipetting with a P1000 pipette. 600,000 live cells were seeded in non tissue culture treated 12-well
747 plates and transduced with high titer lentiviruses at an MOI of 2-5 in the presence of polybrene and ROCK
748 inhibitor. The plates were subsequently centrifuged at 1,000 g for 90 min at RT, followed by overnight
749 incubation. The following morning, 1 ml fresh SCM was added to each well and the cells were gently
750 mixed with a P1000 to dislodge any adhered cells. 48-72 hours after transduction, BFP positive cells
751 were sorted to enrich for transduced cells. After a 24-hour recovery period, cells were used for
752 downstream analyses.
753
754 ***Inhibition of PGC-1α and OXPHOS***
755 For pharmacological inhibition of PGC-1α (with SR-18292) and OXPHOS (with IACS-010759 and
756 IMT1B), 96-well plates were pre-filled with SCM media (described above) containing each of the inhibitors
757 or DMSO as a control. Cell growth was quantified using the Cell Titer-Glo Luminescent Cell Viability
758 Assay (Cat# G7570, Promega) as described below.
759 ***Cell proliferation assay***
760 2,000 - 10,000 cells per cell line in 3-6 replicates were seeded into black, opaque 96-well plates with a
761 glass bottom. Cell content was measured on Days 1-6 using Cell Titer-Glo Luminescent Cell Viability

762 Assay (Cat# G7570, Promega). Luminescence was measured at an integration time of 0.5 second per
763 well. The number of cell doublings were calculated between the day of plating, and the termination of the
764 assay, indicated on each figure panel. Because CTG uses an ATP-based readout, and since the
765 mitochondrial inhibitors influence the amount of ATP in the cell, the internal GFP, driven by the AKT1
766 (FU-myrAKT1-CGW) vector was also quantified using microscopy and a plate reader. Consistent results
767 were obtained with both techniques.
768
769 ***RT-qPCR***
770 Total RNA was isolated from cells using miRNeasy Mini Kit (Cat# 217004, Qiagen). cDNA was
771 synthesized from 2 ug of total RNA using the SuperScript IV First-Strand Synthesis System (Cat#
772 18091050, Thermo Fisher). RT-qPCR was performed using SYBR Green PCR Master Mix (Cat#
773 4309155, Thermo Fisher). Amplification was carried out using the StepOne Real-Time PCR System
774 (Cat# 4376357, Thermo Fisher) and analysis was performed using the StepOne Software v2.3. Relative
775 quantification was determined using the Delta-Delta Ct Method. The following primer pair was used to
776 amplify PGC-1α mRNA:
777 CCTGCTCGGAGCTTCTCAAA
778 CCCTTGGGGTCATTTGGTGA
779
780 ***Tissue section, histology, and immunohistochemistry (IHC)***
781 PARCB tumors were fixed by overnight nutation in 10% buffered formaldehyde (SF100-4) at 4℃ followed
782 by three washes in 70% ethanol. Hematoxylin and eosin (H&E) staining was performed by UCLA's
783 Translation Pathology Core Laboratory (TPCL) using standard protocols. TPCL is a CAP/CLIA certified
784 research facility in the UCLA Department of Pathology and Laboratory Medicine and a UCLA Jonsson
785 Comprehensive Cancer Center Shared Facility. For immunohistochemistry, formalin-fixed, paraffin-
786 embedded (FFPE) PARCB tumors were deparaffinized in xylene and rehydrated. Citrate buffer (pH=6.0)
787 was used for antigen retrieval. The sections were incubated in citrate buffer and heated in a pressure
788 cooker. 3% H2O2 in methanol was used to block endogenous peroxidase activity for 10 min at room

789 temperature. The sections were blocked then incubated with primary antibodies overnight at 4°C. Anti-
790 mouse/rabbit secondary antibodies were used to detect proteins of interest and DAB EqV substrate was
791 used to visualize the staining. All components were included in the ImmPRESS Kit (MP-7801-15 and
792 MP-7802-15, Vector Laboratories). The slides were then dehydrated and mounted with Xylene-based
793 drying medium (Cat# 22-050-262, Fisher Scientific).
794
795 ***Western blot***
796 1 million viable cells were lysed on ice using RIPA lysis buffer (Cat#89900, Thermo Fisher). Protein
797 concentrations were measured using the Pierce BCA Protein Assay Kit (Cat#: 23227, Thermo Scientific).
798 Samples were electrophoresed on polyacrylamide gels (Cat# NW04120BOX, Thermo Fisher),
799 transferred to PVDF membranes (Cat# IPVH00010, Millipore). Western blots were visualized using
800 iBright CL1500 Imaging system (Cat#44114, Thermo Fisher).
801
802 ***Antibodies***
803 The following antibodies were used: PGC-1α ms monoclonal 4C1.3 (Sigma, ST1202), TOMM20 ms
804 monoclonal (Santa Cruz Biotechnology, sc-17764), NCAM1/CD56 (Abcam, ab133345), and OXPHOS
805 cocktail ms monoclonal (Abcam, ab110411).
806
807 ***Bulk RNA sequencing and dataset collection***
808 Tumors were dissociated into single cells, followed by cell sorting of quadruple colors (BFP, GFP, YFP,
809 and RFP) by flow cytometry. Total RNA was extracted from the cell lysates using the Zymo Direct-zol
810 RNA Miniprep Plus Kit (Cat. No: R2072). Quality check was performed on the Agilent 4200 Tapestation
811 (Agilent Technology; cat. no. G2991BA). Libraries for RNA-Seq of PARCB with PGC-1α overexpression
812 and control samples were prepared with KAPA Stranded mRNA-Seq Kit (Cat# KK8420, Roche). The
813 workflow consists of mRNA enrichment and fragmentation. Sequencing was performed on Illumina Hiseq
814 3000 or NovaSeq 6000 for PE 2x150 run. Data quality check was done on Illumina SAV. Demultiplexing
815 was performed with Illumina Bcl2fastq v2.19.1.403 software. Raw sequencing reads were processed

816 through the UCSC TOIL RNA Sequencing pipeline for quality control, adapter trimming, sequence
817 alignment, and expression quantification. Briefly, sequence adapters were trimmed using CutAdapt v1.9,
818 sequences were then aligned to human reference genome GRCh38 using STAR v2.4.2a and gene
819 expression quantification was performed using RSEM v1.2.25 with transcript annotations from
820 GENCODE v23[83].

821 The FASTQ files of the Park dataset[6], Beltran dataset[33], George dataset[32], Rajan dataset[124]
822 (GSE48403), and Chen dataset were all processed through the TOIL pipeline with the same parameters
823 to get RSEM expected counts. The TOIL-RSEM expected counts of TCGA pan cancer samples were
824 obtained directly from UCSC Xena browser (https://xenabrowser.net/datapages) and RSEM read counts
825 of pan-cancer cell lines from the Cancer Cell Line Encyclopedia (CCLE) were downloaded from DepMap
826 Portal (DepMap Public 22Q1) (https://depmap.org/portal/download/all/). The RSEM counts of all
827 combined datasets were upper quartile normalized with a pseudocount of 1 and log2 transformed
828 (referred to as log2 (UQN+1) counts) and filtered down to HUGO protein coding genes
829 (http://www.genenames.org/) for the downstream analyses. SCLC subtypes[43] and CRPC subtypes[54]
830 were previously defined.

831 Sequencing of high-grade serous ovarian carcinomas (HGSOC) was approved through UCLA
832 Institutional Review Board (IRB) approved protocols (IRB #10-000727, IRB #20-001626). Tumor
833 specimens were obtained from high-grade serous ovarian cancer patients who had given their informed
834 consent. RNA was isolated from both solid tumors collected from primary and metastatic sites, and
835 effusion samples such as ascites and pleural fluid. Dissociated or cryopreserved tumor fragments were
836 used for isolation of RNA. These samples were collected at various disease time points: chemonaive,
837 post adjuvant or neoadjuvant chemotherapy, and at disease recurrence. Presence of tumor cells was
838 confirmed on histologic sections. RNA isolation, library preparation, and sequencing were conducted by
839 the Technology Center for Genomics and Bioinformatics (TCGB) core facility at UCLA.

840 ***Differential gene expression analysis and hierarchical clustering***

841 Differential expression analysis was performed on raw RSEM expected count data of protein-coding
842 genes using the R package DESeq2[100].

843

844 ***Gene set enrichment analysis (GSEA) and GSEA-squared***

845 Differential gene expression analysis was first performed on raw RSEM expected count data of protein-
846 coding genes on the Rajan 2014[124] dataset between Pre-ADT and Post-ADT samples.
847 Using the fgsea R package (https://github.com/ctlab/fgsea), gene set enrichment analysis (GSEA) was
848 then performed on the hallmark (H), canonical pathways (CP), and gene ontology (GO) gene sets from
849 MSigDB[101]. Additional mitochondria related gene sets were also included from MitoCarta3.0. The ranked
850 list of genes was generated using the signed log2 fold change and -log10 transformed p-values calculated
851 by DESeq2[102]. GSEA results were then ranked by Normalized Enrichment Score (NES) to identify highly
852 enriched gene sets. To investigate pathways broadly related to our highly enriched gene sets (e.g.,
853 oxidative phosphorylation and adhesion), GSEA-Squared analysis was performed. In short, gene sets
854 were ranked by NES and marked for if they contained a key term from that category of terms in the
855 pathway name. KS tests were then performed using ks.test.2 to assess the distribution of the category
856 of terms[102]. The keys used were the following:

857

858 Oxidative Phosphorylation, OXIDATIVE PHOSPHORYLATION, ELECTRON TRANSPORT,
859 MITOCHONDRIAL COMPLEX, NADH DEHYDROGENASE, MITOCHONDRIAL LARGE RIBOSOMAL;
860 OXPHOS
861 Adhesion, ADHESION, ADHERENS

862

863 Differential gene expression analysis was also performed on raw RSEM expected count data of protein-
864 coding genes on the Chen 2014[32] dataset between HC6/ Class II/ ASCL1+ tumors and the rest of the
865 samples in the dataset. Similar methods were used to perform gene set enrichment analysis on GO BP
866 2021 gene sets from MSigDB, except genes were ranked by their adjusted p-value.

867 ***Principle component analyses***

868 Unsupervised principal component analysis (PCA) was performed on log2 transformed upper quartile
869 normalized RSEM expected count data. The prcomp function in R was run centered and unscaled. Data

870 was projected onto the PCA framework by multiplying the rotation matrix by the projected data's
871 expression matrix.
872
873 ***Small cell neuroendocrine (SCN) score***
874 SCN score was calculated as previously described in Balanis et al[1]. Briefly, PC1 loadings were taken
875 from a pan-cancer PCA which followed non-small cell cancers along their transdifferentiation trajectory
876 towards an SCN phenotype. A higher SCN score indicates a more SCN-like phenotype, while a lower
877 SCN score indicates a more normal, non-SCN-like phenotype.
878
879 ***Motif analysis***
880 ATAC sequencing data was obtained from Chen 2023 dataset[32]. The raw FASTQ files were processed
881 using the published ENCODE ATAC-Seq Pipeline (https://github.com/ENCODE-DCC/atacseq-pipeline).
882 The reads were trimmed and aligned to hg38 using bowtie2. Picard was used to de-duplicate reads,
883 which were then filtered for high-quality paired reads using SAMtools. All peak calling was performed
884 using MACS3. The optimal irreproducible discovery rate (IDR) thresholded peak output was used for all
885 downstream analyses, with a threshold P value of 0.05. Other ENCODE3 parameters were enforced with
886 the flag-encode3. Reads that mapped to mitochondrial genes or blacklisted regions, as defined by the
887 ENCODE pipeline, were removed. The peak files were merged using bedtools merge to create a
888 consensus set of peaks across all samples, and the number of reads in each peak was determined using
889 bedtools multicov[103]. A variance stabilizing transformation was performed on peak counts using
890 DESeq2[100] and batch effects were removed using removeBatchEffect from limma[104]. DESeq2 was then
891 used to variance stabilize transform read counts and determine hyper- and hypo-accessible peaks across
892 HC5 and HC6 PARCB time course samples, using default parameters and without independent filtering
893 or Cook's cutoff. Peaks were called as hyper or hypo-accessible using abs(log2 fold change)>2 and
894 adjusted $p<0.05$. Motif analysis was then run separately on hyper- or hypo-accessible peaks in the HC5
895 versus. HC6 comparison using HOMER[105] with the flags -size 200 and -mask. Motifs were then ranked

896 by their p-value for hyper- or hypo-accessible peak sets. Motifs specific to hyper or hypo accessible
897 peaks were obtained by taking the rank difference of the motifs in the two lists.
898
899 ***Single-cell RNA sequencing***
900 Single-cell expression levels of ASCL1, PGC-1α, ASCL2, and POU2F3 in PARCB time course tumors
901 were extracted from our recently published study[13]. Gene expression was visualized using Uniform
902 Manifold Approximation and Projection (UMAP) analysis as described previously[13]. The downstream
903 quality control, as well as batch integration and correction of PARCB single cell RNA-seq data were
904 performed as described previously[13]. Briefly, visualization of PARCB single cell RNA-seq data was
905 performed using the Seurat (5.0.3) R package[106]. The top 30 principal components were used to perform
906 UMAP analysis. Cell clustering was performed with FindNeighbors function with top 30 principal
907 components and FindClusters function with resolution of 0.5.
908
909 ***Seahorse respirometry***
910 Respirometry experiments were performed on a Seahorse XF96 Extracellular Flux Analyzer (Agilent
911 Technologies). PARCB tumor-derived cell lines were process and counted as described, washed into
912 Seahorse Assay medium (Seahorse XF Base Medium supplemented with 2 mM L-glutamine, 1 mM
913 pyruvate and 10 mM glucose) and immediately seeded into an XF96 microplate, pre-coated with PDL.
914 Cells were plated at a density of 40,000 cells per well in a final volume of 175 µl. Prior to the start of the
915 assay, the XF96 plate was placed in a 37 °C incubator without CO2 for 30 min. During the assay, the
916 following compounds were injected: the mitochondrial ATP synthase inhibitor oligomycin (final
917 concentration 2 µM); the mitochondrial uncoupler FCCP (final concentration 1 µM); and the complex I
918 and III inhibitors rotenone (final concentration 2 µM); and the complex III inhibitor antimycin A (final
919 concentration 2 µM). At the conclusion of the assay, the cells were fixed with 4% paraformaldehyde,
920 stained with Hoechst, and cell number per well was determine based on nuclei number using an Operetta
921 High-Content Imaging System (PerkinElmer). OCRs were normalized to cell number per well.
922

923 **microPET/CT imaging of tumor metabolism**

924 Tumor-bearing mice were injected with 60 μCi of [^{18}F]-FDG (PETNET Solutions) or [^{18}F]-BnTP (prepared
925 as previously described[107] through tail vein intravenous injections. Following a 60-minute unconscious
926 uptake of the imaging tracer, mice were anesthetized with 2% vaporized isoflurane, and microPET
927 (energy window 350-650 keV, 10-min static scan) and microCT (voltage 80 kVp, current 150 μA, 720
928 projections, 200μm resolution, scan time 1 min) images were acquired on a GNEXT PET/CT scanner
929 (Sofie Biosciences, Dulles, VA). The microPET images were reconstructed using a 3D-Ordered Subset
930 Expectation Maximization (OSEM) algorithm (24 subsets and 3 iterations), with random, attenuation, and
931 decay correction. The microCT images were reconstructed using a Modified Feldkamp Algorithm. Amide
932 software was used to analyze co-registered microPET/CT images. Representative maximum-intensity-
933 projection (MIP) images are shown.

934

935 **Chromatin immunoprocepticiation sequencing (ChIP-Seq)**

936 To analyze the regulatory impact of ASCL1 on PGC-1α, we utilized Chromatin Immunoprecipitation
937 Sequencing (ChIP-Seq) data from several studies, including Augustyn et al., 2014 (GSE61197),
938 Borromeo et al., 2016 (GSE69398), Cejas et al., 2021 (GSE156290), and Nouruzi et al., 2022
939 (GSE183198), which were downloaded directly from the Gene Expression Omnibus (GEO). We
940 converted data from bedGraph and wig formats to bigWig format using the UCSC bedGraphToBigWig
941 and wigToBigWig tools to standardize data representation. To align all datasets to a consistent reference
942 genome, we lifted data initially mapped to hg19 over to hg38 using the UCSC liftOver tool. For the Li et
943 al., 2024 ChIP-Seq dataset, we merged bigWig files from replicates at each timepoint using the UCSC
944 bigWigMerge tool, aiming to consolidate data for comprehensive analysis. Visualization of the processed
945 datasets was performed with the Integrative Genomics Viewer (IGV 2.17.1), ensuring uniform
946 background noise levels across samples to facilitate accurate comparison.

947 **SUPPLEMENTAL FIGURE LEGENDS**

948 **Figure S1.** Related to Figure 1.

949 A. Related to Figure 1A. Gene expression analysis of PGC-1α versus the SCNC lineage markers
950 POU2F3, NEUROD1, and YAP1 in all the human cancer cell lines from the cancer cell line
951 encyclopedia (CCLE).
952 B. Related to Figure 1A. PGC-1α expression levels in non-small cell lung cancer (NSCLC), small
953 cell lung cancer (SCLC), and neuroblastoma (NB) cell lines from the CCLE.
954 C. Co-expression analysis of PGC-1α and ASCL1 in all tumor samples from The Cancer Genome
955 Atlas (TCGA).
956 D. Co-expression analysis of PGC-1α and ASCL1 in a cohort of patients with high-grade serous
957 ovarian carcinomas (HGSOC).
958
959 The data for Figure S1B are presented as mean ± SEM, with statistical significance denoted by ***
960 ($p \leq 0.001$). The green lines represent the best-fit linear regression model, with the indicated R^2 and p-
961 values. All Log2 values are Log2 UQN+1. For statistical tests used, see Material and Methods section
962
963 **Figure S2.** Related to Figure 2.
964 Expression levels of PGC-1α vs ASCL1, POU2F3, ASCL2 expression in single cells from the PARCB
965 time course tumors from Chen et al. 2023[13].
966
967 **Figure S3.** Related to Figure 3
968 Cell proliferation analysis of PARCB tumor-derived cell lines treated with SR-18292, a
969 pharmacological inhibitor of PGC-1α.
970
971 **Figure S4.** Related to Figure 5
972 A. Western blot analysis of PGC-1α overexpression effects on the expression levels of all five
973 respiratory chain complexes in a panel of 4 PARCB tumor-derived cell lines. The PARCB cell
974 lines were generated previously[2]

975 B. H&E staining in tumor sections from POU2F3/ASCL2 and ASCL1 PARCB tumors with PGC-1α
976 overexpression and control. These tumors were generated from terminally differentiated PARCB
977 cell lines re-injected into mice for tumor growth, as described in Figure 5. Note the increased
978 vasculature of POU2F3/ASCL2 tumors upon PGC-1α overexpression. Scale bars are 60 μm.
979
980 **Figure S5.** Related to Figure 6
981 A. PGC-1α mRNA levels using RT-qPCR in PARCB organoids with PGC-1α overexpression versus
982 control. Organoids were harvested just before xenografting.
983 B. Flow cytometry and fluorescence microscopy analysis of PARCB tumors with PGC-1α
984 overexpression and control. The PGC-1α overexpression and control constructs include a blue
985 fluorescence protein encoded by EBFP2. See Materials and Methods section for more details.
986 C. Western blot analysis of PGC-1α protein levels in PARCB tumors with PGC-1α overexpression
987 versus control. HEK 293T cells overexpressing PGC-1α were included as an additional control.
988
989 **Figure S6.** Related to Figure 7
990 ASCL1 ChiP-Seq analyses showing the alternative promoter of PGC-1α corresponding to variant
991 X2 (XM_005248132.1) encoded by exon1b. The following datasets were used: SCN lung cancer
992 cell lines[81,82], SCN prostate cancer cell lines[64,80], and LuCaP prostate cancer patient-derived
993 xenografts (PDXs)[12].
994
995 **Figure S7.** Related to Figure 7
996 ASCL1 ChiP-Seq analyses highlighting variant 1 of PGC-1α (NM_001330751.2) (red box). The
997 following datasets were used: SCN lung cancer cell lines[81,82], SCN prostate cancer cell lines[64,80],
998 and LuCaP prostate cancer patient-derived xenografts (PDXs)[12].
999
1000 **Figure S8.** Related to Figure 7

1001 ASCL1 ChiP-Seq analyses indicating a region within the PGC-1α gene body. The following datasets were
1002 used: SCN lung cancer cell lines81,82, SCN prostate cancer cell lines64,80, and LuCaP prostate cancer
1003 patient-derived xenografts (PDXs)12.

1004 **REFERENCES**

1005 1. Balanis, N. G. *et al.* Pan-cancer Convergence to a Small-Cell Neuroendocrine Phenotype that
1006 Shares Susceptibilities with Hematological Malignancies. *Cancer Cell* **36**, 17-34.e7 (2019).
1007 2. Park, J. W. *et al.* Reprogramming normal human epithelial tissues to a common, lethal
1008 neuroendocrine cancer lineage. *Science* **362**, 91–95 (2018).
1009 3. Wang, L. *et al.* A genetically defined disease model reveals that urothelial cells can initiate
1010 divergent bladder cancer phenotypes. *Proceedings of the National Academy of Sciences* **117**, 563–
1011 572 (2020).
1012 4. Oberg, K. *et al.* Consensus on biomarkers for neuroendocrine tumour disease. *The Lancet*
1013 *Oncology* **16**, e435–e446 (2015).
1014 5. Zhang, Y. *et al.* Androgen deprivation promotes neuroendocrine differentiation and angiogenesis
1015 through CREB-EZH2-TSP1 pathway in prostate cancers. *Nat Commun* **9**, 4080 (2018).
1016 6. Li, Y. *et al.* SRRM4 Drives Neuroendocrine Transdifferentiation of Prostate Adenocarcinoma Under
1017 Androgen Receptor Pathway Inhibition. *European Urology* **71**, 68–78 (2017).
1018 7. Nadal, R., Schweizer, M., Kryvenko, O. N., Epstein, J. I. & Eisenberger, M. A. Small cell carcinoma
1019 of the prostate. *Nat Rev Urol* **11**, 213–219 (2014).
1020 8. Aggarwal, R. *et al.* Clinical and Genomic Characterization of Treatment-Emergent Small-Cell
1021 Neuroendocrine Prostate Cancer: A Multi-institutional Prospective Study. *JCO* **36**, 2492–2503
1022 (2018).
1023 9. Ireland, A. S. *et al.* MYC Drives Temporal Evolution of Small Cell Lung Cancer Subtypes by
1024 Reprogramming Neuroendocrine Fate. *Cancer Cell* **38**, 60-78.e12 (2020).
1025 10. Sutherland, K. D., Ireland, A. S. & Oliver, T. G. Killing SCLC: insights into how to target a
1026 shapeshifting tumor. *Genes Dev* **36**, 241–258 (2022).
1027 11. Brady, N. J. *et al.* Temporal evolution of cellular heterogeneity during the progression to advanced
1028 AR-negative prostate cancer. *Nat Commun* **12**, 3372 (2021).
1029 12. Cejas, P. *et al.* Subtype heterogeneity and epigenetic convergence in neuroendocrine prostate
1030 cancer. *Nat Commun* **12**, 5775 (2021).
1031 13. Chen, C.-C. *et al.* Temporal evolution reveals bifurcated lineages in aggressive neuroendocrine
1032 small cell prostate cancer trans-differentiation. *Cancer Cell* **41**, 2066-2082.e9 (2023).
1033 14. Chan, J. M. *et al.* Lineage plasticity in prostate cancer depends on JAK/STAT inflammatory
1034 signaling. *Science* **377**, 1180–1191 (2022).
1035 15. Mu, P. *et al.* SOX2 promotes lineage plasticity and antiandrogen resistance in TP53- and RB1-
1036 deficient prostate cancer. *Science* **355**, 84–88 (2017).
1037 16. Huang, F. *et al.* Inosine Monophosphate Dehydrogenase Dependence in a Subset of Small Cell
1038 Lung Cancers. *Cell Metab* **28**, 369-382.e5 (2018).
1039 17. Chalishazar, M. D. *et al.* MYC-Driven Small-Cell Lung Cancer is Metabolically Distinct and
1040 Vulnerable to Arginine Depletion. *Clinical Cancer Research* **25**, 5107–5121 (2019).
1041 18. Zhang, C., Shang, X. & Wang, H. Untargeted metabolomics and lipidomics identified four subtypes
1042 of small cell lung cancer. *Metabolomics* **19**, 3 (2022).
1043 19. Kim, J. & DeBerardinis, R. J. Mechanisms and implications of metabolic heterogeneity in cancer.
1044 *Cell Metab* **30**, 434–446 (2019).
1045 20. Szeitz, B. *et al.* In-depth proteomic analysis reveals unique subtype-specific signatures in human
1046 small-cell lung cancer. *Clinical and Translational Medicine* **12**, e1060 (2022).
1047 21. Nagarajan, A., Malvi, P. & Wajapeyee, N. Oncogene-Directed Alterations in Cancer Cell
1048 Metabolism. *Trends in Cancer* **2**, 365–377 (2016).
1049 22. Folmes, C. D. L., Dzeja, P. P., Nelson, T. J. & Terzic, A. Metabolic Plasticity in Stem Cell
1050 Homeostasis and Differentiation. *Cell Stem Cell* **11**, 596–606 (2012).
1051 23. Morrish, F. & Hockenbery, D. MYC and Mitochondrial Biogenesis. *Cold Spring Harb Perspect Med*
1052 **4**, a014225 (2014).
1053 24. Chen, J. *et al.* MYC-driven increases in mitochondrial DNA copy number occur early and persist
1054 throughout prostatic cancer progression. *bioRxiv* 2023.02.20.529259 (2023)
1055 doi:10.1101/2023.02.20.529259.

1056 25. Purhonen, J., Klefström, J. & Kallijärvi, J. MYC—an emerging player in mitochondrial diseases.
1057 *Frontiers in Cell and Developmental Biology* **11**, (2023).
1058 26. Sancho, P. *et al.* MYC/PGC-1α Balance Determines the Metabolic Phenotype and Plasticity of
1059 Pancreatic Cancer Stem Cells. *Cell Metabolism* **22**, 590–605 (2015).
1060 27. Stine, Z. E., Walton, Z. E., Altman, B. J., Hsieh, A. L. & Dang, C. V. MYC, Metabolism, and Cancer.
1061 *Cancer Discovery* **5**, 1024–1039 (2015).
1062 28. Hoxhaj, G. & Manning, B. D. The PI3K–AKT network at the interface of oncogenic signalling and
1063 cancer metabolism. *Nature Reviews Cancer* **20**, 74–88 (2020).
1064 29. Whiteman, E. L., Cho, H. & Birnbaum, M. J. Role of Akt/protein kinase B in metabolism. *Trends in*
1065 *Endocrinology & Metabolism* **13**, 444–451 (2002).
1066 30. Zhang, C. *et al.* Tumour-associated mutant p53 drives the Warburg effect. *Nat Commun* **4**, 2935
1067 (2013).
1068 31. Aquilano, K. *et al.* p53 Orchestrates the PGC-1α-Mediated Antioxidant Response Upon Mild Redox
1069 and Metabolic Imbalance. *Antioxid Redox Signal* **18**, 386–399 (2013).
1070 32. Zacksenhaus, E. *et al.* Mitochondrial OXPHOS induced by RB1 deficiency in breast cancer:
1071 implications for anabolic metabolism, stemness, and metastasis. *Trends in cancer* **3**, 768–779
1072 (2017).
1073 33. Conroy, L. R. *et al.* Loss of Rb1 enhances glycolytic metabolism in Kras-driven lung tumors in vivo.
1074 *Cancers* **12**, 237 (2020).
1075 34. Clem, B. F. & Chesney, J. Molecular pathways: regulation of metabolism by RB. *Clinical Cancer*
1076 *Research* **18**, 6096–6100 (2012).
1077 35. Warburg, O., Wind, F. & Negelein, E. THE METABOLISM OF TUMORS IN THE BODY. *J Gen*
1078 *Physiol* **8**, 519–530 (1927).
1079 36. Warburg, O. On the origin of cancer cells. *Science* **123**, 309–314 (1956).
1080 37. Vander Heiden, M. G., Cantley, L. C. & Thompson, C. B. Understanding the Warburg Effect: The
1081 Metabolic Requirements of Cell Proliferation. *Science* **324**, 1029–1033 (2009).
1082 38. Faubert, B., Solmonson, A. & DeBerardinis, R. J. Metabolic reprogramming and cancer
1083 progression. *Science* **368**, eaaw5473 (2020).
1084 39. Vasan, K., Werner, M. & Chandel, N. S. Mitochondrial Metabolism as a Target for Cancer Therapy.
1085 *Cell Metabolism* **32**, 341–352 (2020).
1086 40. Vander Heiden, M. G. & DeBerardinis, R. J. Understanding the Intersections between Metabolism
1087 and Cancer Biology. *Cell* **168**, 657–669 (2017).
1088 41. Farge, T. *et al.* Chemotherapy-Resistant Human Acute Myeloid Leukemia Cells Are Not Enriched
1089 for Leukemic Stem Cells but Require Oxidative Metabolism. *Cancer Discovery* **7**, 716–735 (2017).
1090 42. Guièze, R. *et al.* Mitochondrial Reprogramming Underlies Resistance to BCL-2 Inhibition in
1091 Lymphoid Malignancies. *Cancer Cell* **36**, 369-384.e13 (2019).
1092 43. Viale, A. *et al.* Oncogene ablation-resistant pancreatic cancer cells depend on mitochondrial
1093 function. *Nature* **514**, 628–632 (2014).
1094 44. Bosc, C., Selak, M. A. & Sarry, J.-E. Resistance Is Futile: Targeting Mitochondrial Energetics and
1095 Metabolism to Overcome Drug Resistance in Cancer Treatment. *Cell Metabolism* **26**, 705–707
1096 (2017).
1097 45. Kuntz, E. M. *et al.* Targeting mitochondrial oxidative phosphorylation eradicates therapy-resistant
1098 chronic myeloid leukemia stem cells. *Nat Med* **23**, 1234–1240 (2017).
1099 46. Pendleton, K. E., Wang, K. & Echeverria, G. V. Rewiring of mitochondrial metabolism in therapy-
1100 resistant cancers: permanent and plastic adaptations. *Frontiers in Cell and Developmental Biology*
1101 **11**, (2023).
1102 47. Molina, J. R. *et al.* An inhibitor of oxidative phosphorylation exploits cancer vulnerability. *Nat Med*
1103 **24**, 1036–1046 (2018).
1104 48. Wheaton, W. W. *et al.* Metformin inhibits mitochondrial complex I of cancer cells to reduce
1105 tumorigenesis. *eLife* **3**, e02242 (2014).
1106 49. Evans, K. W. *et al.* Oxidative Phosphorylation Is a Metabolic Vulnerability in Chemotherapy-
1107 Resistant Triple-Negative Breast Cancer. *Cancer Research* **81**, 5572–5581 (2021).
1108 50. Choi, S. Y. C. *et al.* Targeting MCT4 to reduce lactic acid secretion and glycolysis for treatment of
1109 neuroendocrine prostate cancer. *Cancer Med* (2018) doi:10.1002/cam4.1587.

51. Puigserver, P. & Spiegelman, B. M. Peroxisome Proliferator-Activated Receptor-γ Coactivator 1α (PGC-1α): Transcriptional Coactivator and Metabolic Regulator. *Endocrine Reviews* **24**, 78–90 (2003).
52. Puigserver, P. *et al.* A Cold-Inducible Coactivator of Nuclear Receptors Linked to Adaptive Thermogenesis. *Cell* **92**, 829–839 (1998).
53. Luo, C., Widlund, H. R. & Puigserver, P. PGC-1 Coactivators: Shepherding the Mitochondrial Biogenesis of Tumors. *Trends in Cancer* **2**, 619–631 (2016).
54. Tennakoon, J. B. *et al.* Androgens regulate prostate cancer cell growth via an AMPK-PGC-1α-mediated metabolic switch. *Oncogene* **33**, 5251–5261 (2014).
55. Shiota, M. *et al.* Peroxisome proliferator-activated receptor gamma coactivator-1alpha interacts with the androgen receptor (AR) and promotes prostate cancer cell growth by activating the AR. *Mol Endocrinol* **24**, 114–127 (2010).
56. Kaminski, L. *et al.* PGC1α Inhibits Polyamine Synthesis to Suppress Prostate Cancer Aggressiveness. *Cancer Research* **79**, 3268–3280 (2019).
57. Valcarcel-Jimenez, L. *et al.* PGC1α Suppresses Prostate Cancer Cell Invasion through ERRα Transcriptional Control. *Cancer Research* **79**, 6153–6165 (2019).
58. Torrano, V. *et al.* The metabolic co-regulator PGC1α suppresses prostate cancer metastasis. *Nat Cell Biol* **18**, 645–656 (2016).
59. Vazquez, F. *et al.* PGC1α expression defines a subset of human melanoma tumors with increased mitochondrial capacity and resistance to oxidative stress. *Cancer Cell* **23**, 287–301 (2013).
60. Luo, C. *et al.* A PGC1α-mediated transcriptional axis suppresses melanoma metastasis. *Nature* **537**, 422–426 (2016).
61. Oh, T.-I. *et al.* PGC1α Loss Promotes Lung Cancer Metastasis through Epithelial-Mesenchymal Transition. *Cancers (Basel)* **13**, 1772 (2021).
62. LeBleu, V. S. *et al.* PGC-1α mediates mitochondrial biogenesis and oxidative phosphorylation in cancer cells to promote metastasis. *Nat Cell Biol* **16**, 992–1003 (2014).
63. Borges, M. *et al.* An achaete-scute homologue essential for neuroendocrine differentiation in the lung. *Nature* **386**, 852–855 (1997).
64. Nouruzi, S. *et al.* ASCL1 activates neuronal stem cell-like lineage programming through remodeling of the chromatin landscape in prostate cancer. *Nat Commun* **13**, 2282 (2022).
65. García-Bellido, A. & Santamaria, P. Developmental Analysis of the Achaete-Scute System of DROSOPHILA MELANOGASTER. *Genetics* **88**, 469–486 (1978).
66. The Cancer Genome Atlas Program (TCGA) - NCI. https://www.cancer.gov/ccg/research/genome-sequencing/tcga (2022).
67. Beltran, H. *et al.* Divergent clonal evolution of castration-resistant neuroendocrine prostate cancer. *Nat Med* **22**, 298–305 (2016).
68. George, J. *et al.* Comprehensive genomic profiles of small cell lung cancer. *Nature* **524**, 47–53 (2015).
69. Cancer Genome Atlas Research Network. Integrated genomic analyses of ovarian carcinoma. *Nature* **474**, 609–615 (2011).
70. Rajan, P. *et al.* Next-generation Sequencing of Advanced Prostate Cancer Treated with Androgen-deprivation Therapy. *European Urology* **66**, 32–39 (2014).
71. Divakaruni, A. S., Paradyse, A., Ferrick, D. A., Murphy, A. N. & Jastroch, M. Chapter Sixteen - Analysis and Interpretation of Microplate-Based Oxygen Consumption and pH Data. in *Methods in Enzymology* (eds. Murphy, A. N. & Chan, D. C.) vol. 547 309–354 (Academic Press, 2014).
72. Bricker, D. K. *et al.* A Mitochondrial Pyruvate Carrier Required for Pyruvate Uptake in Yeast, Drosophila, and Humans. *Science* **337**, 96–100 (2012).
73. Miller, K. N., Clark, J. P. & Anderson, R. M. Mitochondrial regulator PGC-1a—Modulating the modulator. *Current Opinion in Endocrine and Metabolic Research* **5**, 37–44 (2019).
74. Jannig, P. R., Dumesic, P. A., Spiegelman, B. M. & Ruas, J. L. SnapShot: Regulation and biology of PGC-1α. *Cell* **185**, 1444-1444.e1 (2022).
75. Sharabi, K. *et al.* Selective Chemical Inhibition of PGC-1α Gluconeogenic Activity Ameliorates Type 2 Diabetes. *Cell* **169**, 148-160.e15 (2017).
76. Tsherniak, A. *et al.* Defining a Cancer Dependency Map. *Cell* **170**, 564-576.e16 (2017).

1164 77. Seo, B. B. *et al.* Molecular remedy of complex I defects: Rotenone-insensitive internal NADH-
1165 quinone oxidoreductase of Saccharomyces cerevisiae mitochondria restores the NADH oxidase
1166 activity of complex I-deficient mammalian cells. *Proceedings of the National Academy of Sciences*
1167 **95**, 9167–9171 (1998).
1168 78. Bonekamp, N. A. *et al.* Small-molecule inhibitors of human mitochondrial DNA transcription. *Nature*
1169 **588**, 712–716 (2020).
1170 79. Dart, A. Mapping out mitochondria. *Nat Rev Cancer* **23**, 273–273 (2023).
1171 80. Li, S. *et al.* Defined cellular reprogramming of androgen receptor-active prostate cancer to
1172 neuroendocrine prostate cancer. *Cell Reports* (In review).
1173 81. Augustyn, A. *et al.* ASCL1 is a lineage oncogene providing therapeutic targets for high-grade
1174 neuroendocrine lung cancers. *Proceedings of the National Academy of Sciences* **111**, 14788–
1175 14793 (2014).
1176 82. Borromeo, M. D. *et al.* ASCL1 and NEUROD1 Reveal Heterogeneity in Pulmonary Neuroendocrine
1177 Tumors and Regulate Distinct Genetic Programs. *Cell Rep* **16**, 1259–1272 (2016).
1178 83. Basu, H. S. *et al.* Prostate cancer cells survive anti-androgen and mitochondrial metabolic inhibitors
1179 by modulating glycolysis and mitochondrial metabolic activities. *Prostate* **81**, 799–811 (2021).
1180 84. Crowell, P. D. *et al.* MYC is a regulator of androgen receptor inhibition-induced metabolic
1181 requirements in prostate cancer. *Cell Rep* **42**, 113221 (2023).
1182 85. Yap, T. A. *et al.* Phase I trial of IACS-010759 (IACS), a potent, selective inhibitor of complex I of the
1183 mitochondrial electron transport chain, in patients (pts) with advanced solid tumors. *JCO* **37**, 3014–
1184 3014 (2019).
1185 86. M.D. Anderson Cancer Center. *Phase 1 Study of IACS-010759 in Subjects With Relapsed or*
1186 *Refractory AML*. https://clinicaltrials.gov/ct2/show/NCT02882321 (2022).
1187 87. Tsuji, A., Akao, T., Masuya, T., Murai, M. & Miyoshi, H. IACS-010759, a potent inhibitor of
1188 glycolysis-deficient hypoxic tumor cells, inhibits mitochondrial respiratory complex I through a
1189 unique mechanism. *J Biol Chem* **295**, 7481–7491 (2020).
1190 88. Yap, T. A. *et al.* Complex I inhibitor of oxidative phosphorylation in advanced solid tumors and
1191 acute myeloid leukemia: phase I trials. *Nat Med* **29**, 115–126 (2023).
1192 89. Zhang, X. & Dang, C. V. Time to hit pause on mitochondria-targeting cancer therapies. *Nat Med* **29**,
1193 29–30 (2023).
1194 90. Dominy, J. E. *et al.* The deacetylase Sirt6 activates the acetyltransferase GCN5 and suppresses
1195 hepatic gluconeogenesis. *Mol Cell* **48**, 900–913 (2012).
1196 91. Lerin, C. *et al.* GCN5 acetyltransferase complex controls glucose metabolism through
1197 transcriptional repression of PGC-1alpha. *Cell Metab* **3**, 429–438 (2006).
1198 92. Xiang, Y. *et al.* SR18292 exerts potent antitumor effects in multiple myeloma via inhibition of
1199 oxidative phosphorylation. *Life Sci* **256**, 117971 (2020).
1200 93. de Visser, K. E. & Joyce, J. A. The evolving tumor microenvironment: From cancer initiation to
1201 metastatic outgrowth. *Cancer Cell* **41**, 374–403 (2023).
1202 94. Sharp, A. *et al.* Clinical Utility of Circulating Tumour Cell Androgen Receptor Splice Variant-7
1203 Status in Metastatic Castration-resistant Prostate Cancer. *European Urology* **76**, 676–685 (2019).
1204 95. Abida, W. *et al.* Genomic correlates of clinical outcome in advanced prostate cancer. *Proceedings*
1205 *of the National Academy of Sciences* **116**, 11428–11436 (2019).
1206 96. Labrecque, M. P. *et al.* Molecular profiling stratifies diverse phenotypes of treatment-refractory
1207 metastatic castration-resistant prostate cancer. *J Clin Invest* **129**, 4492–4505 (2019).
1208 97. Beltran, H. *et al.* The Role of Lineage Plasticity in Prostate Cancer Therapy Resistance. *Clinical*
1209 *Cancer Research* **25**, 6916–6924 (2019).
1210 98. Szklarczyk, D. *et al.* The STRING database in 2023: protein-protein association networks and
1211 functional enrichment analyses for any sequenced genome of interest. *Nucleic Acids Res* **51**,
1212 D638–D646 (2023).
1213 99. Momcilovic, M. *et al.* In vivo imaging of mitochondrial membrane potential in non-small-cell lung
1214 cancer. *Nature* **575**, 380–384 (2019).
1215 100. Love, M. I., Huber, W. & Anders, S. Moderated estimation of fold change and dispersion for
1216 RNA-seq data with DESeq2. *Genome Biol* **15**, 550 (2014).

1217 101. Liberzon, A. *et al.* Molecular signatures database (MSigDB) 3.0. *Bioinformatics* **27**, 1739–1740
1218 (2011).
1219 102. Subramanian, A. *et al.* Gene set enrichment analysis: a knowledge-based approach for
1220 interpreting genome-wide expression profiles. *Proc Natl Acad Sci U S A* **102**, 15545–15550 (2005).
1221 103. Quinlan, A. R. & Hall, I. M. BEDTools: a flexible suite of utilities for comparing genomic features.
1222 *Bioinformatics* **26**, 841–842 (2010).
1223 104. Ritchie, M. E. *et al.* limma powers differential expression analyses for RNA-sequencing and
1224 microarray studies. *Nucleic Acids Res* **43**, e47 (2015).
1225 105. Heinz, S. *et al.* Simple combinations of lineage-determining transcription factors prime cis-
1226 regulatory elements required for macrophage and B cell identities. *Mol Cell* **38**, 576–589 (2010).
1227 106. Hao, Y. *et al.* Dictionary learning for integrative, multimodal and scalable single-cell analysis.
1228 *Nat Biotechnol* **42**, 293–304 (2024).
1229 107. Han, M. *et al.* Spatial mapping of mitochondrial networks and bioenergetics in lung cancer.
1230 *Nature* **615**, 712–719 (2023).
1231

Figure 1

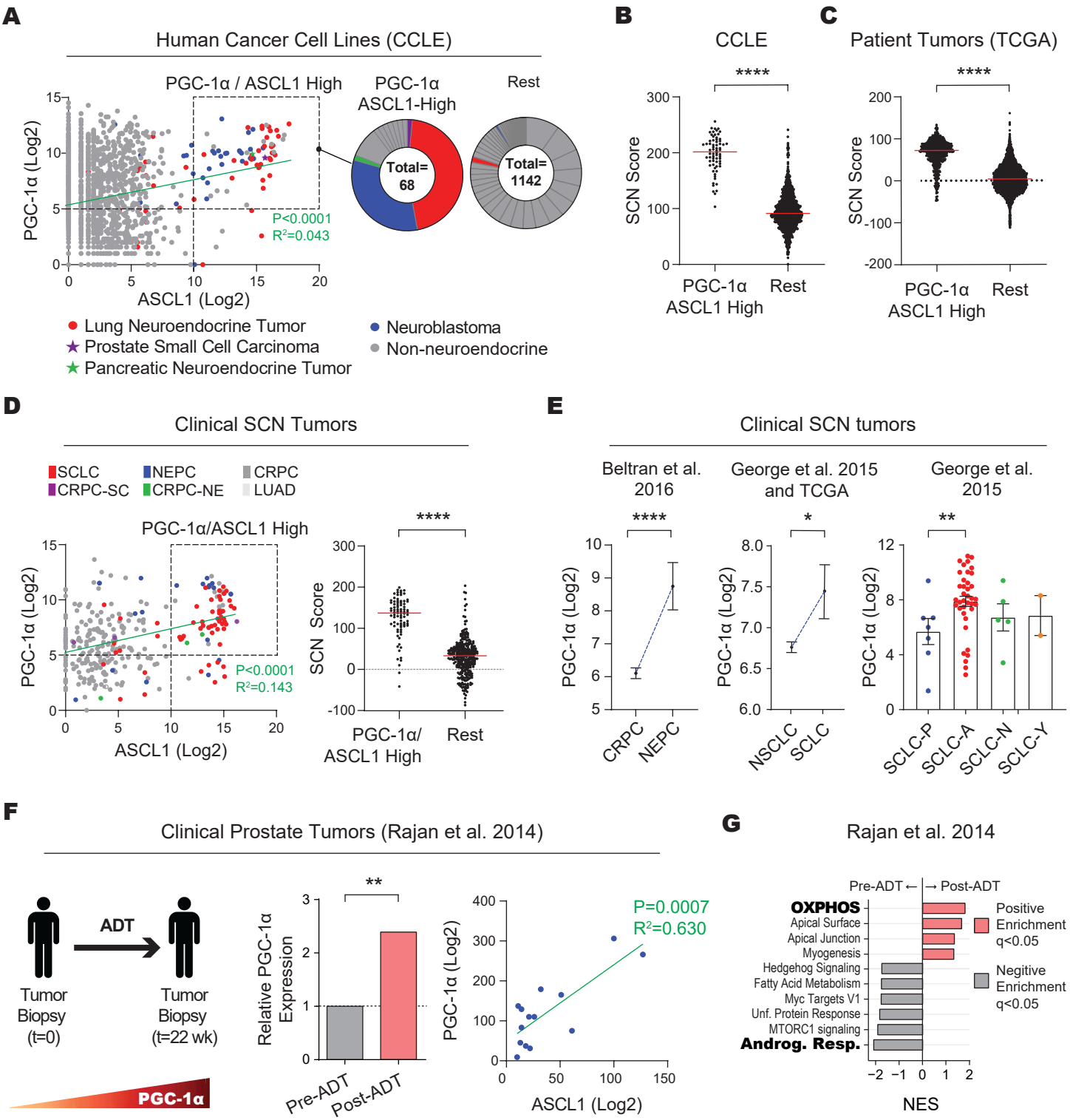
A
Human Cancer Cell Lines (CCLE)
PGC-1α / ASCL1 High
PGC-1α ASCL1-High
Rest
Total= 68
Total= 1142
P<0.0001
R²=0.043
PGC-1α (Log2)
ASCL1 (Log2)
Lung Neuroendocrine Tumor
Prostate Small Cell Carcinoma
Pancreatic Neuroendocrine Tumor
Neuroblastoma
Non-neuroendocrine
B
CCLE
SCN Score
PGC-1α ASCL1 High
Rest
C
Patient Tumors (TCGA)
D
Clinical SCN Tumors
SCLC
NEPC
CRPC
CRPC-SC
CRPC-NE
LUAD
PGC-1α/ASCL1 High
P<0.0001
R²=0.143
E
Clinical SCN tumors
Beltran et al. 2016
George et al. 2015 and TCGA
George et al. 2015
CRPC
NEPC
NSCLC
SCLC
SCLC-P
SCLC-A
SCLC-N
SCLC-Y
F
Clinical Prostate Tumors (Rajan et al. 2014)
ADT
Tumor Biopsy (t=0)
Tumor Biopsy (t=22 wk)
PGC-1α
Relative PGC-1α Expression
Pre-ADT
Post-ADT
P=0.0007
R²=0.630
G
Rajan et al. 2014
Pre-ADT ← → Post-ADT
OXPHOS
Apical Surface
Apical Junction
Myogenesis
Hedgehog Signaling
Fatty Acid Metabolism
Myc Targets V1
Unf. Protein Response
MTORC1 signaling
Androg. Resp.
Positive Enrichment q<0.05
Negitive Enrichment q<0.05
NES

Figure 2

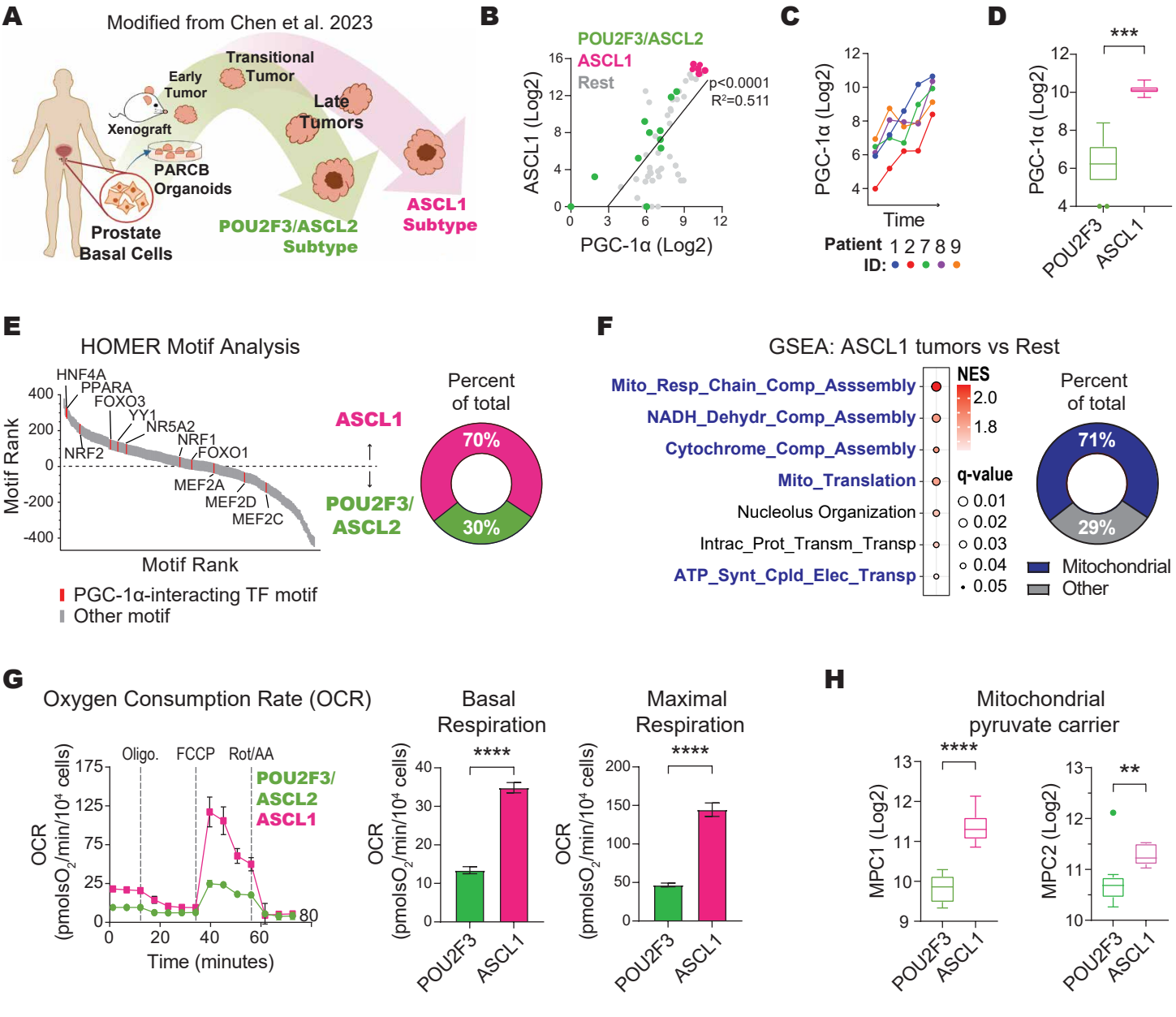
A
Modified from Chen et al. 2023
Transitional Tumor
Early Tumor
Xenograft
Late Tumors
PARCB Organoids
Prostate Basal Cells
POU2F3/ASCL2 Subtype
ASCL1 Subtype
B
POU2F3/ASCL2
ASCL1
Rest
p<0.0001
R²=0.511
ASCL1 (Log2)
PGC-1α (Log2)
C
PGC-1α (Log2)
Time
Patient ID: 1 2 7 8 9
D
***
PGC-1α (Log2)
POU2F3
ASCL1
E
HOMER Motif Analysis
HNF4A
PPARA
FOXO3
YY1
NR5A2
NRF1
FOXO1
NRF2
MEF2A
MEF2D
MEF2C
Motif Rank
ASCL1
POU2F3/ASCL2
Percent of total
70%
30%
PGC-1α-interacting TF motif
Other motif
F
GSEA: ASCL1 tumors vs Rest
Mito_Resp_Chain_Comp_Asssembly
NADH_Dehydr_Comp_Assembly
Cytochrome_Comp_Assembly
Mito_Translation
Nucleolus Organization
Intrac_Prot_Transm_Transp
ATP_Synt_Cpld_Elec_Transp
NES
q-value
Percent of total
71%
29%
Mitochondrial
Other
G
Oxygen Consumption Rate (OCR)
Oligo.
FCCP
Rot/AA
POU2F3/ASCL2
ASCL1
OCR (pmolsO2/min/10⁴ cells)
Time (minutes)
Basal Respiration
Maximal Respiration
****
POU2F3
ASCL1
H
Mitochondrial pyruvate carrier
MPC1 (Log2)
MPC2 (Log2)
****
**
POU2F3
ASCL1

Figure 3

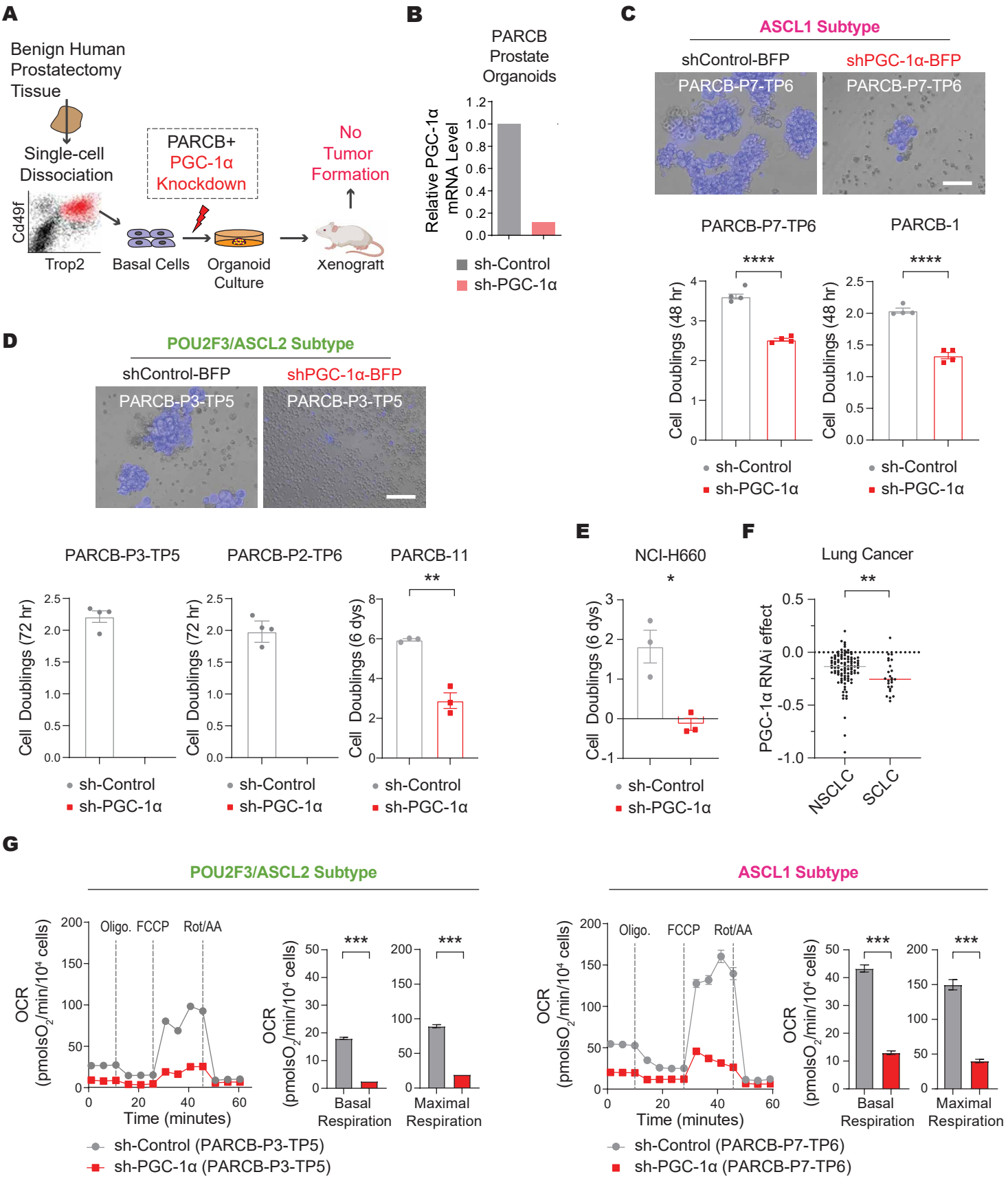
A
Benign Human Prostatectomy Tissue
Single-cell Dissociation
Cd49f
Trop2
Basal Cells
PARCB+ PGC-1α Knockdown
Organoid Culture
Xenograft
No Tumor Formation
B
PARCB Prostate Organoids
Relative PGC-1α mRNA Level
sh-Control
sh-PGC-1α
C
ASCL1 Subtype
shControl-BFP
shPGC-1α-BFP
PARCB-P7-TP6
PARCB-P7-TP6
PARCB-P7-TP6
PARCB-1
Cell Doublings (48 hr)
****
****
sh-Control
sh-PGC-1α
D
POU2F3/ASCL2 Subtype
shControl-BFP
shPGC-1α-BFP
PARCB-P3-TP5
PARCB-P3-TP5
PARCB-P3-TP5
PARCB-P2-TP6
PARCB-11
Cell Doublings (72 hr)
Cell Doublings (6 dys)
**
sh-Control
sh-PGC-1α
E
NCI-H660
*
Cell Doublings (6 dys)
sh-Control
sh-PGC-1α
F
Lung Cancer
**
PGC-1α RNAi effect
NSCLC
SCLC
G
POU2F3/ASCL2 Subtype
OCR (pmolsO2/min/10^4 cells)
Oligo.
FCCP
Rot/AA
Time (minutes)
***
***
Basal Respiration
Maximal Respiration
sh-Control (PARCB-P3-TP5)
sh-PGC-1α (PARCB-P3-TP5)
ASCL1 Subtype
Oligo.
FCCP
Rot/AA
Time (minutes)
***
***
Basal Respiration
Maximal Respiration
sh-Control (PARCB-P7-TP6)
sh-PGC-1α (PARCB-P7-TP6)

Figure 4

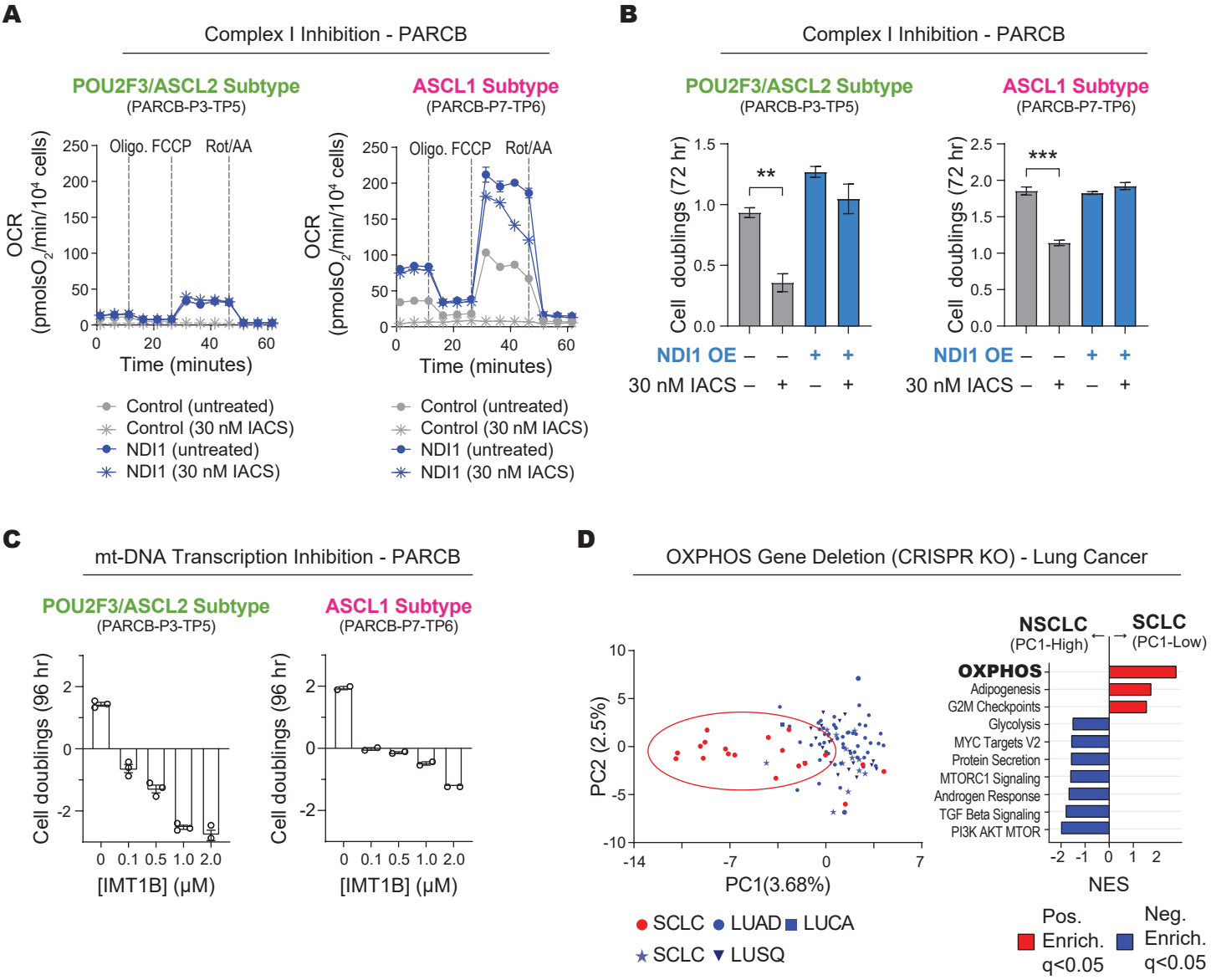
A
Complex I Inhibition - PARCB
POU2F3/ASCL2 Subtype
(PARCB-P3-TP5)
ASCL1 Subtype
(PARCB-P7-TP6)
OCR (pmolsO2/min/10^4 cells)
Oligo. FCCP Rot/AA
Time (minutes)
Control (untreated)
Control (30 nM IACS)
NDI1 (untreated)
NDI1 (30 nM IACS)
B
Complex I Inhibition - PARCB
POU2F3/ASCL2 Subtype
(PARCB-P3-TP5)
ASCL1 Subtype
(PARCB-P7-TP6)
Cell doublings (72 hr)
NDI1 OE
30 nM IACS
C
mt-DNA Transcription Inhibition - PARCB
POU2F3/ASCL2 Subtype
(PARCB-P3-TP5)
ASCL1 Subtype
(PARCB-P7-TP6)
Cell doublings (96 hr)
[IMT1B] (μM)
D
OXPHOS Gene Deletion (CRISPR KO) - Lung Cancer
PC2 (2.5%)
PC1(3.68%)
SCLC LUAD LUCA
SCLC LUSQ
NSCLC (PC1-High)
SCLC (PC1-Low)
OXPHOS
Adipogenesis
G2M Checkpoints
Glycolysis
MYC Targets V2
Protein Secretion
MTORC1 Signaling
Androgen Response
TGF Beta Signaling
PI3K AKT MTOR
NES
Pos. Enrich. q<0.05
Neg. Enrich. q<0.05

Figure 5

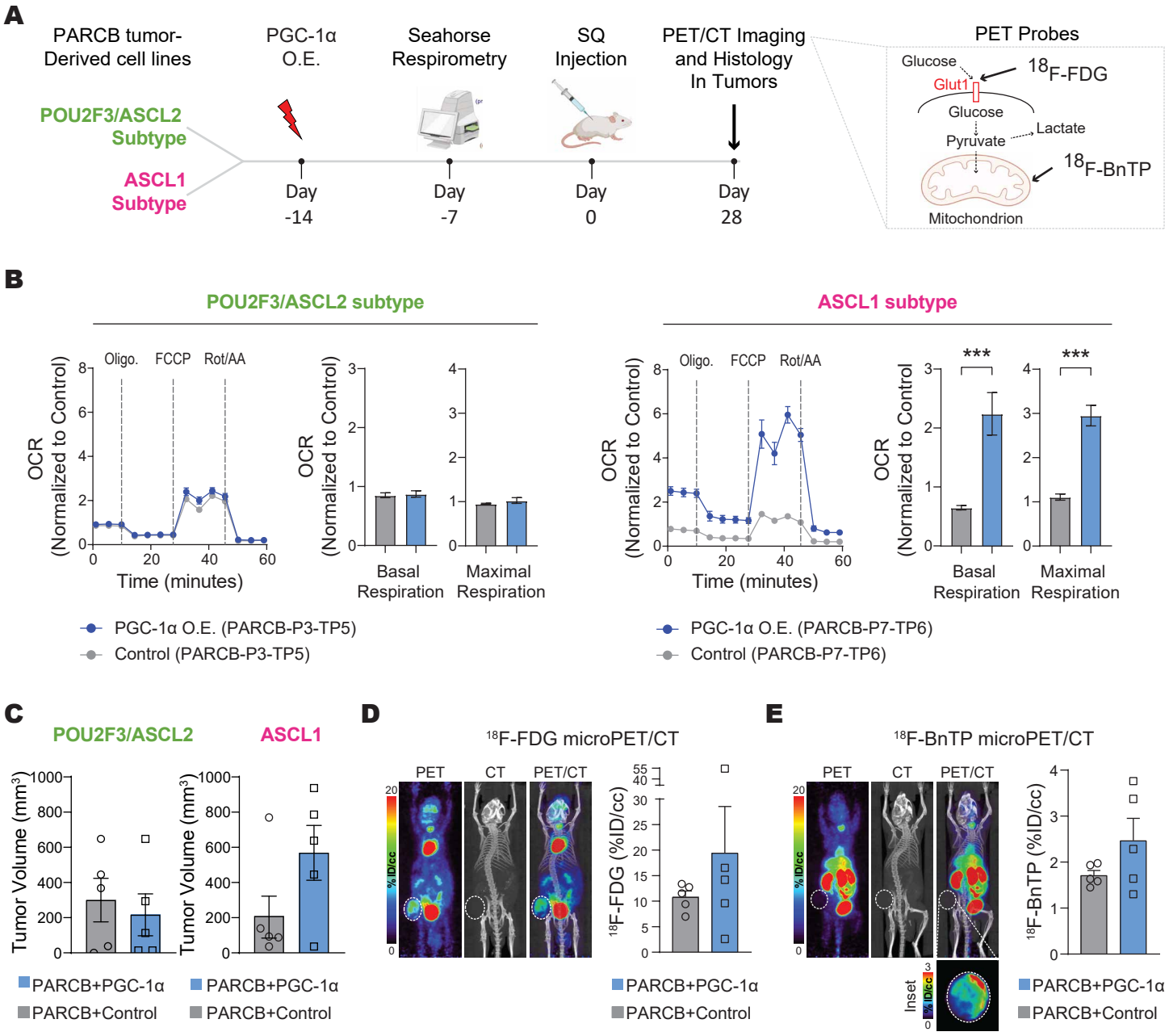
A
PARCB tumor-Derived cell lines
PGC-1α O.E.
Seahorse Respirometry
SQ Injection
PET/CT Imaging and Histology In Tumors
PET Probes
POU2F3/ASCL2 Subtype
ASCL1 Subtype
Day -14
Day -7
Day 0
Day 28
Glucose
Glut1
18F-FDG
Glucose
Lactate
Pyruvate
18F-BnTP
Mitochondrion
B
POU2F3/ASCL2 subtype
ASCL1 subtype
Oligo.
FCCP
Rot/AA
OCR (Normalized to Control)
Time (minutes)
Basal Respiration
Maximal Respiration
***
PGC-1α O.E. (PARCB-P3-TP5)
Control (PARCB-P3-TP5)
PGC-1α O.E. (PARCB-P7-TP6)
Control (PARCB-P7-TP6)
C
POU2F3/ASCL2
ASCL1
Tumor Volume (mm3)
PARCB+PGC-1α
PARCB+Control
D
18F-FDG microPET/CT
PET
CT
PET/CT
%ID/cc
18F-FDG (%ID/cc)
PARCB+PGC-1α
PARCB+Control
E
18F-BnTP microPET/CT
PET
CT
PET/CT
%ID/cc
Inset
18F-BnTP (%ID/cc)
PARCB+PGC-1α
PARCB+Control

Figure 6

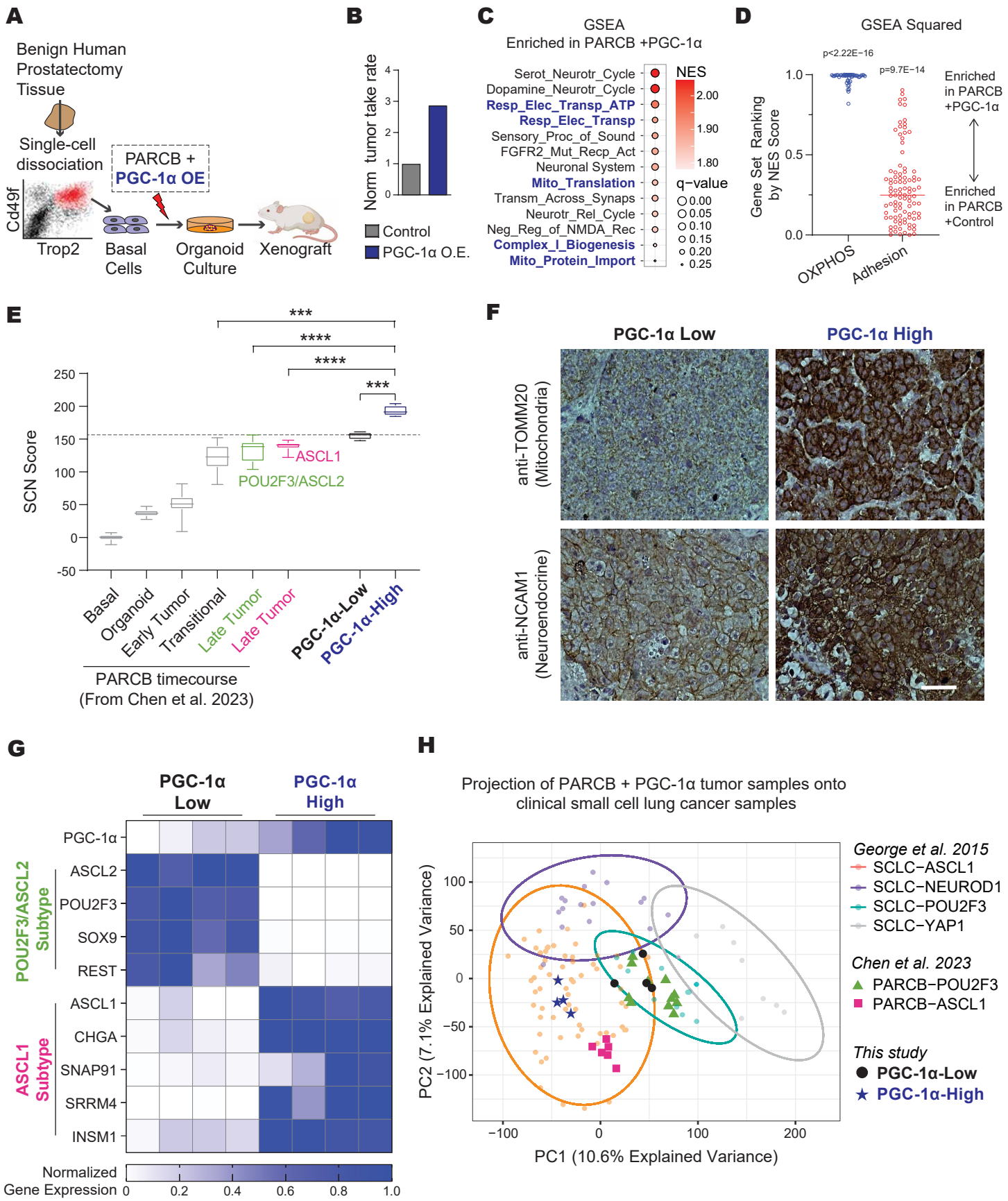
A
Benign Human Prostatectomy Tissue
Single-cell dissociation
PARCB + PGC-1α OE
Cd49f
Trop2
Basal Cells
Organoid Culture
Xenograft
B
Norm tumor take rate
Control
PGC-1α O.E.
C
GSEA
Enriched in PARCB +PGC-1α
Serot_Neurotr_Cycle
Dopamine_Neurotr_Cycle
Resp_Elec_Transp_ATP
Resp_Elec_Transp
Sensory_Proc_of_Sound
FGFR2_Mut_Recp_Act
Neuronal System
Mito_Translation
Transm_Across_Synaps
Neurotr_Rel_Cycle
Neg_Reg_of_NMDA_Rec
Complex_I_Biogenesis
Mito_Protein_Import
NES
q−value
D
GSEA Squared
p<2.22E−16
p=9.7E−14
Gene Set Ranking by NES Score
Enriched in PARCB +PGC-1α
Enriched in PARCB +Control
OXPHOS
Adhesion
E
SCN Score
ASCL1
POU2F3/ASCL2
Basal
Organoid
Early Tumor
Transitional
Late Tumor
Late Tumor
PGC-1α-Low
PGC-1α-High
PARCB timecourse
(From Chen et al. 2023)
F
PGC-1α Low
PGC-1α High
anti-TOMM20 (Mitochondria)
anti-NCAM1 (Neuroendocrine)
G
PGC-1α Low
PGC-1α High
PGC-1α
POU2F3/ASCL2 Subtype
ASCL2
POU2F3
SOX9
REST
ASCL1 Subtype
ASCL1
CHGA
SNAP91
SRRM4
INSM1
Normalized Gene Expression
H
Projection of PARCB + PGC-1α tumor samples onto clinical small cell lung cancer samples
PC2 (7.1% Explained Variance)
PC1 (10.6% Explained Variance)
George et al. 2015
SCLC−ASCL1
SCLC−NEUROD1
SCLC−POU2F3
SCLC−YAP1
Chen et al. 2023
PARCB−POU2F3
PARCB−ASCL1
This study
PGC-1α-Low
PGC-1α-High

Figure 7

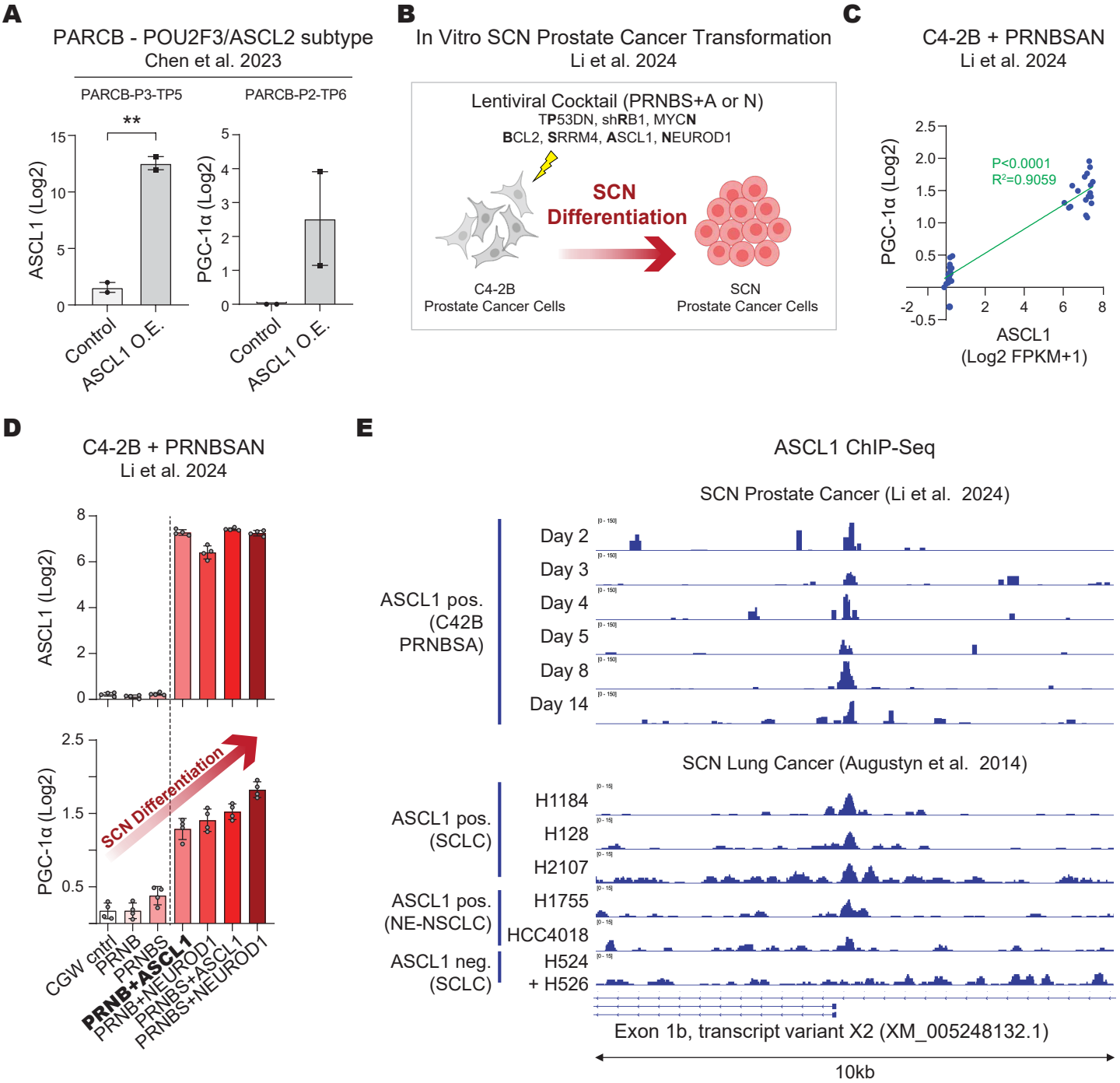
A
PARCB - POU2F3/ASCL2 subtype
Chen et al. 2023
PARCB-P3-TP5
PARCB-P2-TP6
**
ASCL1 (Log2)
PGC-1α (Log2)
Control
ASCL1 O.E.
B
In Vitro SCN Prostate Cancer Transformation
Li et al. 2024
Lentiviral Cocktail (PRNBS+A or N)
TP53DN, shRB1, MYCN
BCL2, SRRM4, ASCL1, NEUROD1
SCN Differentiation
C4-2B Prostate Cancer Cells
SCN Prostate Cancer Cells
C
C4-2B + PRNBSAN
Li et al. 2024
P<0.0001
R²=0.9059
PGC-1α (Log2)
ASCL1 (Log2 FPKM+1)
D
C4-2B + PRNBSAN
Li et al. 2024
ASCL1 (Log2)
PGC-1α (Log2)
SCN Differentiation
CGW cntrl
PRNB
PRNBS
PRNB+ASCL1
PRNB+NEUROD1
PRNBS+ASCL1
PRNBS+NEUROD1
E
ASCL1 ChIP-Seq
SCN Prostate Cancer (Li et al. 2024)
ASCL1 pos. (C42B PRNBSA)
Day 2
Day 3
Day 4
Day 5
Day 8
Day 14
SCN Lung Cancer (Augustyn et al. 2014)
ASCL1 pos. (SCLC)
H1184
H128
H2107
ASCL1 pos. (NE-NSCLC)
H1755
HCC4018
ASCL1 neg. (SCLC)
H524 + H526
Exon 1b, transcript variant X2 (XM_005248132.1)
10kb